
Quantum manipulation on the Barium quadrupolar transition

A diploma thesis in physics
submitted to the
FACULTY OF MATHEMATICS, COMPUTER SCIENCE AND PHYSICS
UNIVERSITY OF INNSBRUCK

In partial fulfilment of the requirements for the degree of
MASTER OF NATURAL SCIENCE
MAGISTER RERUM NATURALIUM

by
NADIA RÖCK

Supervisor
PROF. DR. RAINER BLATT
DEPARTMENT OF EXPERIMENTAL PHYSICS

August 2011

FÜR MEINEN KLEINEN BRUDER,
DER MICH DIE WELT MIT ANDEREN AUGEN SEHEN LÄSST

Abstract

This thesis reports on the setup and stabilization of a new fiber laser system to manipulate the Barium quadrupolar transition, with the aim to enable coherent control of the ion's internal and motional quantum state.

The experiments are performed with a single Barium ion trapped in a linear Paul trap and Doppler cooled to the Lamb Dicke regime. The narrow quadrupolar transition between the $|S_{1/2}\rangle$ and $|D_{5/2}\rangle$ states is used for state preparation, manipulation and readout.

The implementation of the laser system allowed first observations of quantum jumps and Rabi oscillations in this setup, as well as quantum state spectroscopy on the quadrupole transition. Furthermore, we present with this apparatus a first performance of sideband cooling to about 65 % ground state probability.

Contents

Introduction	6
1 The Barium experiment	8
1.1 The Barium ion	8
1.1.1 Electronic structure	8
1.1.2 The Zeeman effect	10
1.2 Former experiments	11
1.2.1 QED-effects	11
1.2.2 Towards remote entanglement	12
2 Ion motion in a Paul trap	14
2.1 Principle of the Paul trap	14
2.2 The linear Paul trap	15
3 Trapped ion coupled to a laser field	18
3.1 Light-matter interaction	18
3.1.1 Time evolution and Rabi flopping	21
3.1.2 State detection via electron shelving	22
3.2 Laser cooling	24
3.2.1 Doppler cooling	24
3.2.2 Sideband cooling	25
4 Experimental setup	27
4.1 Vacuum vessel and linear trap setup	28
4.2 Laser systems	32
4.2.1 Frequency doubled 1.2 μm repumping laser	33
4.2.2 Laser for the quadrupole transition at 1.7 μm	36
4.3 Generating experimental sequences	38
4.4 Intensity stabilization of the 1.7 μm laser	40
4.4.1 Characterization of the laser intensity fluctuations	40
4.4.2 Basic principle of feedback control	41
4.4.3 Experimental realization and results	43

5	Locking of the 1.7 μm laser to a high finesse cavity	46
5.1	Cavity design and setup	46
5.2	Characterization of the cavity for the 1.7 μm laser	49
5.2.1	Cavity parameters	49
5.2.2	Temperature dependence	51
5.3	Pound-Drever-Hall frequency stabilization	53
5.3.1	The Pound-Drever-Hall technique	53
5.3.2	Experimental realization and results	55
6	Spectroscopy and sideband cooling on a single $^{138}\text{Ba}^+$	58
6.1	Quantum jumps using the fiber laser	58
6.2	Spectroscopy on the $ S_{1/2}\rangle$ to $ D_{5/2}\rangle$ transition	60
6.3	Rabi oscillations	64
6.4	Sideband cooling	66
7	Summary and outlook	69
A	The quadrupole transition	75
B	Doppler cooling limit	77
C	Feedback control theory	79
D	Pound-Drever-Hall error signal	81
E	Phyton sequence for pulse generation	83

List of Figures

1.1	Level scheme for $^{138}\text{Ba}^+$	9
1.2	Degeneracy and Zeeman splitting of the fine structure states	10
1.3	Experimental setup for light interference measurements from single Barium ions and their mirror images	11
1.4	Experimental setup for the measurement of quantum interference of remotely trapped ions	12
2.1	Scheme of a linear Paul trap	15
3.1	Energy level diagram for carrier, first red and blue sideband excitations	20
3.2	Fluorescence readout of the atomic state via electron shelving	23
3.3	Energy level diagram for sideband cooling	25
4.1	Overview of the experimental apparatus	27
4.2	Sketch of the vacuum vessel with linear Paul trap and photograph of the experimental flange	28
4.3	Photograph and scheme of the linear Paul trap with trap dimensions	29
4.4	Trap geometry and angle between $1.7\ \mu\text{m}$ laser and the individual trap axes	30
4.5	Schematic of the frequency doubled $1.2\ \mu\text{m}$ laser system	34
4.6	Optical setup of the $1.2\ \mu\text{m}$ laser system	35
4.7	Optical setup of the $1.7\ \mu\text{m}$ laser system	37
4.8	Schematic setup of the programmable pulse generator	38
4.9	Dependence of the position of the 80 MHz peak on the laser power	41
4.10	Block diagram illustrating a feedback control system	42
4.11	Schematic setup of the intensity stabilization for the $1.7\ \mu\text{m}$ laser	43
4.12	Intensity noise spectrum up to 3 kHz with and without stabilization	44
4.13	Intensity fluctuations on timescales of minutes with and without stabilization	45
5.1	Design of the high finesse cavity	47
5.2	Photographs of the cavity spacer and vacuum housing	47
5.3	Cavity ring-down measurement to determine the finesse	50

5.4	Measurement of the cavity drift as a function of the temperature	51
5.5	Calculated error signal	54
5.6	Laser setup for PDH locking to the cavity	55
5.7	Measured PDH error signal	56
5.8	Power spectral density of the in-loop error signal	57
6.1	Quantum jumps on the $ S_{1/2}\rangle \longleftrightarrow D_{5/2}\rangle$ transition	59
6.2	Laser pulse sequence used for spectroscopy on the quadrupole transition.	60
6.3	Allowed transitions between the Zeeman sub-levels of the $ S_{1/2}\rangle$ state and $ D_{5/2}\rangle$ state.	61
6.4	Spectrum of the $ S_{1/2}\rangle \longleftrightarrow D_{5/2}\rangle$ transition	62
6.5	Combined linewidth of the laser and magnetic field	63
6.6	Rabi oscillations after Doppler cooling on the $ S_{1/2}\rangle \longleftrightarrow D_{5/2}\rangle$ carrier transition	64
6.7	Laser pulse sequence for sideband cooling	66
6.8	Red axial sideband before and after sideband cooling	67
6.9	Blue axial sideband before and after sideband cooling	67

List of Tables

1.1	Barium isotopes, their mass and nuclear spin	8
1.2	Wavelengths and Einstein-A coefficients of the fine-structure transitions of $^{138}\text{Ba}^+$	9
4.1	Settings of the control gain according to the Ziegler-Nichols method . .	43

Introduction

“One never realizes experiments with a single electron or an atom or a small molecule. In thought experiments, one assumes that sometimes this is possible; invariably, this leads to ridiculous consequences... One may say that one does not realize experiments with single particles, more than one raises ichthyosaurs in the zoo.”[1]

This quote of Erwin Schrödinger dates back to the year 1952 and it highlights how big the development in experimental quantum physics has been within the last nearly 60 years. While then it was not even imaginable, nowadays it is not only possible to experiment with individual atoms, but it is a common tool for investigations of fundamental aspects of quantum mechanics.

Experimenting with single ions and making use of their quantum mechanical properties is of great interest for quantum information processing and quantum cryptography. Already in 1982 Richard Feynman discussed the possibility of simulating interesting physical systems with quantum computers and since then it has become a growing field of research aiming to implement new computational quantum algorithms that would allow one to increase the processing speed or to break encryptions based on classical techniques. In addition to that, single ions are also employed in experiments performing high precision spectroscopy or testing fundamental quantum electrodynamics effects. Their results allow a better understanding of the properties of quantum systems and can therefore lead to new applications.

For all these purposes it is important to have a well controlled quantum system, which means that one needs to be able to prepare a well defined quantum state, realize the desired manipulations and then perform reliable state readout. In the case of trapped ions the internal and external degrees of freedom of the ion are controlled with laser systems coupling different electronic levels. The so called qubit states, used for quantum information processing, can be realized using long lived Zeeman or Hyperfine sub-levels. Narrow transitions from the ground state to this qubit state can be enabled by radio frequency pulses, Raman transitions or very narrow band laser systems driving electric quadrupole transitions. This qubit transition is needed for sideband cooling the ion close to its motional ground state and therefore improves state preparation and allows a better localization of the ion.

In this thesis the setup and stabilization of a narrow band laser system resonant with the $|S_{1/2}\rangle \longleftrightarrow |D_{5/2}\rangle$ quadrupole transition of $^{138}\text{Ba}^+$ will be presented and it will be shown how it can be used for state preparation, manipulation and readout. The structure of the thesis is the following: After giving a general overview over the experiment (Chap. 1) a theoretical part follows explaining the principle of ion trapping (Chap. 2) and

basic atom-light interactions and cooling techniques (Chap. 3). In chapter 4 the experimental setup and the laser systems are presented while chapter 5 describes the locking of the laser to an external reference cavity by the Pound-Drever-Hall technique. Finally the measurements performed with the new laser system are presented (Chap.6) and an outlook for future experiments and further improvements is given (Chap.7).

Chapter 1

The Barium experiment

1.1 The Barium ion

All the measurements discussed within this thesis were performed with single ionized ^{138}Ba atoms. In this first chapter the atomic properties and the electronic structure of Barium are presented. An overview of significant experiments that have been performed in the Barium laboratory is also given to highlight the technical improvements that this thesis can bring to the project.

1.1.1 Electronic structure

The element Barium ($_{56}\text{Ba}$) belongs to the group of the alkaline earth metals. Due to its high reactivity with oxygen and other elements in nature it is never found in its pure form. There exist 22 known Barium isotopes, most of which are highly radioactive. Naturally occurring Barium consists of a mixture of seven stable isotopes. They are listed with their mass, nuclear spin and natural abundance in Tab.1.1.

Isotope	Mass [amu]	Abundance [%]	Nuclear spin [\hbar]
^{130}Ba	129.906282	0.11	0
^{132}Ba	131.905042	0.10	0
^{134}Ba	133.904486	2.42	0
^{135}Ba	134.905665	6.59	$\frac{3}{2}$
^{136}Ba	135.904553	7.85	0
^{137}Ba	136.905812	11.23	$\frac{3}{2}$
^{138}Ba	137.905232	71.70	0

Table 1.1: Natural distribution of the seven stable Barium isotopes, their mass and nuclear spin [2].

All the experiments discussed in this thesis were performed with single ionized ^{138}Ba atoms with the following ground state electron configuration [2]

$$1s^2 2s^2 2p^6 3s^2 3p^6 3d^{10} 4s^2 4p^6 4d^{10} 5s^2 5p^6 6s^1 \quad {}^2S_{1/2} \quad (1.1)$$

This corresponds to the chemical structure of the noble gas Xenon with one additional valence electron $[\text{Xe}] 6s^1$, thus the Barium ion can be considered as a quasi one-electron-system [3]. ^{138}Ba has no nuclear spin, so there is no Hyperfine splitting of the atomic states. This leads to the fine-structure shown in Fig.1.1 for the lowest relevant electronic transitions.

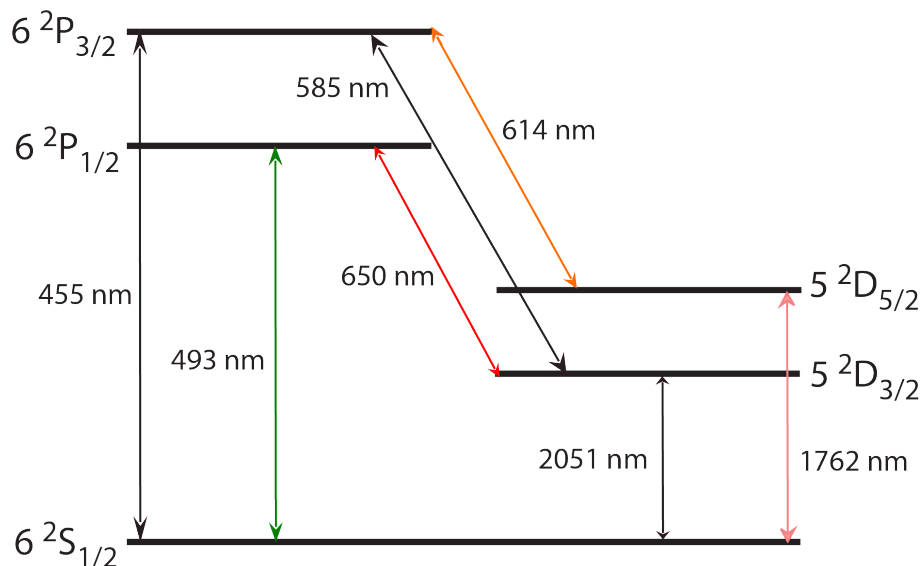


Figure 1.1: Level scheme of the 5 lowest electronic states of $^{138}\text{Ba}^+$ and their corresponding transition wavelengths [2].

The transitions shown in Fig.1.1 are dipole transitions, except of $|S_{1/2}\rangle \longleftrightarrow |D_{3/2}\rangle$ and $|S_{1/2}\rangle \longleftrightarrow |D_{5/2}\rangle$ which are dipole forbidden. Since the atom will there absorb/emit two units of angular momentum, they are electronic quadrupole transitions. The $|S_{1/2}\rangle \longleftrightarrow |D_{5/2}\rangle$ transition will be extensively studied in this thesis.

Transition	λ_{air} [nm]	A_{exp} [$10^6 s^{-1}$]
$6^2S_{1/2} \longleftrightarrow 6^2P_{3/2}$	455.4	118 ± 8
$6^2S_{1/2} \longleftrightarrow 6^2P_{1/2}$	493.4	95 ± 7
$5^2D_{3/2} \longleftrightarrow 6^2P_{3/2}$	585.4	4.8 ± 0.6
$5^2D_{5/2} \longleftrightarrow 6^2P_{3/2}$	614.2	37 ± 4
$5^2D_{3/2} \longleftrightarrow 6^2P_{1/2}$	649.7	33 ± 4
$6^2S_{1/2} \longleftrightarrow 5^2D_{5/2}$	1761.7	$(29 \pm 3) \times 10^{-9}$
$6^2S_{1/2} \longleftrightarrow 5^2D_{3/2}$	2051.2	$(12.5 \pm 0.7) \times 10^{-9}$

Table 1.2: Wavelengths and Einstein-A coefficients of the fine-structure transitions of $^{138}\text{Ba}^+$ [2, 4, 5, 6].

Four laser systems are available to excite the $|S_{1/2}\rangle \longleftrightarrow |P_{1/2}\rangle$, $|D_{5/2}\rangle \longleftrightarrow |P_{3/2}\rangle$, $|D_{3/2}\rangle \longleftrightarrow |P_{1/2}\rangle$ and $|S_{1/2}\rangle \longleftrightarrow |D_{5/2}\rangle$ transitions. The green 493 nm laser is used for Doppler cooling and state detection of the ion. If the ion is excited from the $|S_{1/2}\rangle$ to the $|P_{1/2}\rangle$ it can either decay back to the $|S_{1/2}\rangle$ or into the $|D_{3/2}\rangle$ state with a branching ratio of 3:1 as shown in Tab.1.2. The $|D_{3/2}\rangle$ state has a life-time of about 80 seconds, before it spontaneously decays to the $|S_{1/2}\rangle$ state, therefore the red 650 nm laser is

needed to repump the ion back to the $|P_{1/2}\rangle$ state for efficient cooling. Just as the 650 nm laser brings the ion back to the $|S_{1/2}\rangle$ level, the 614 nm laser is used to repump the ion from the $|D_{5/2}\rangle$ to the $|P_{3/2}\rangle$ state respectively, from where it spontaneously decays back to the $|S_{1/2}\rangle$ state.

1.1.2 The Zeeman effect

Without external magnetic field the fine structure states are degenerate and the quantization axis can be defined by the polarization of the electric field. Therefore, when we excite the atom with linearly polarized light only transitions with $\Delta m_j = 0$ are allowed. Due to spontaneous decay, states with higher Δm_j can also be populated, but cannot be repumped, as can be seen in Fig 1.2(a). Optical pumping into "dark states" with $m_j = \pm 3/2$ makes it impossible to constantly cool the ion [7]. This can either be avoided by applying a weak magnetic field externally or by applying σ^+ and σ^- polarized light.

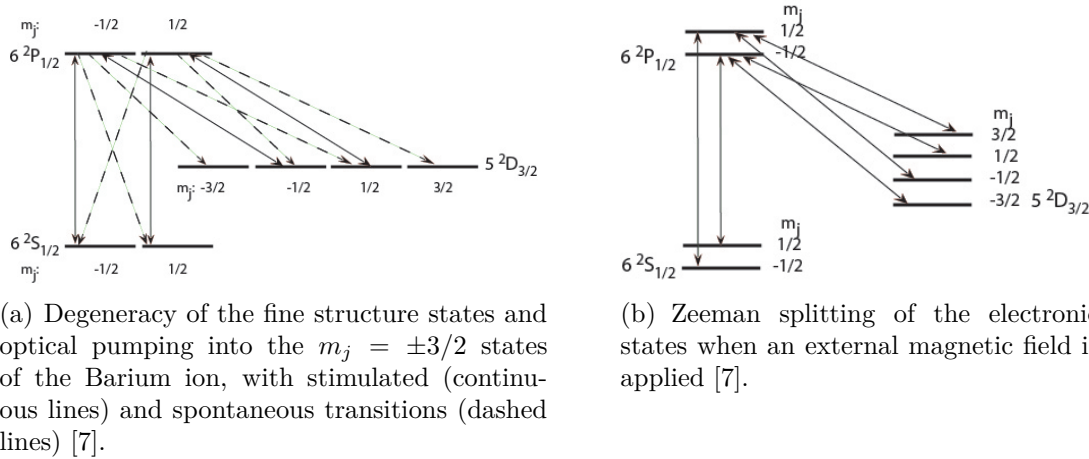


Figure 1.2: Degeneracy of the fine structure states and Zeeman splitting of them with an applied external magnetic field, respectively.

With magnetic field the Zeeman effect causes a splitting of the degenerate fine structure states into $(2j + 1)$ states with the following energy difference [8]

$$\Delta E = g_j \mu_B |B| \quad (1.2)$$

where $\mu_B = \frac{e\hbar}{2m_e}$ is the Bohr magneton and g_j is the Landé g-factor given by

$$g_j = 1 + \frac{j(j+1) + s(s+1) - l(l+1)}{2j(j+1)}. \quad (1.3)$$

The quantization axis is now defined along the direction of the magnetic field. If the polarization of the electric fields is chosen to be perpendicular to this axis, only transitions with $\Delta m_j = \pm 1$ will be driven [7], as shown in Fig. 1.2(b). The ion population is then continuously shuffled and we can cool it easily with linearly polarized and copropagating green and red laser fields.

1.2 Former experiments

The primary goals of the Barium project until now have been the investigation of quantum electrodynamics theory and remote entanglement with well localized atoms. For this purpose several experiments have been performed since its startup at the end of the nineties. I will briefly mention the most important steps performed in this direction.

1.2.1 QED-effects

One important observation was the interference of light emitted by single trapped Barium ions and their mirror images, as depicted in Fig. 1.3. For this measurement the ion was continuously excited and laser cooled on the $|P_{1/2}\rangle \leftrightarrow |D_{3/2}\rangle$ and the $|S_{1/2}\rangle \leftrightarrow |P_{1/2}\rangle$ transition. The 650 nm laser was tuned close to resonance, whereas the 493 nm laser was red detuned by about one transition linewidth Γ for Doppler cooling. The fluorescence from a solid angle of $\sim 4\%$ was collimated with a high-quality lens L2 and sent to a mirror, which retro-reflected the 493 nm part of this light while transmitting the 650 nm part. The retro-reflected light was focused again by L2 to the ion and, together with the light emitted directly into that direction, it was collected by a second lens L1 and recorded on a photomultiplier (PM1). The distance between the mirror and the ion was scanned using a piezo translator (PZT) [9, 10].

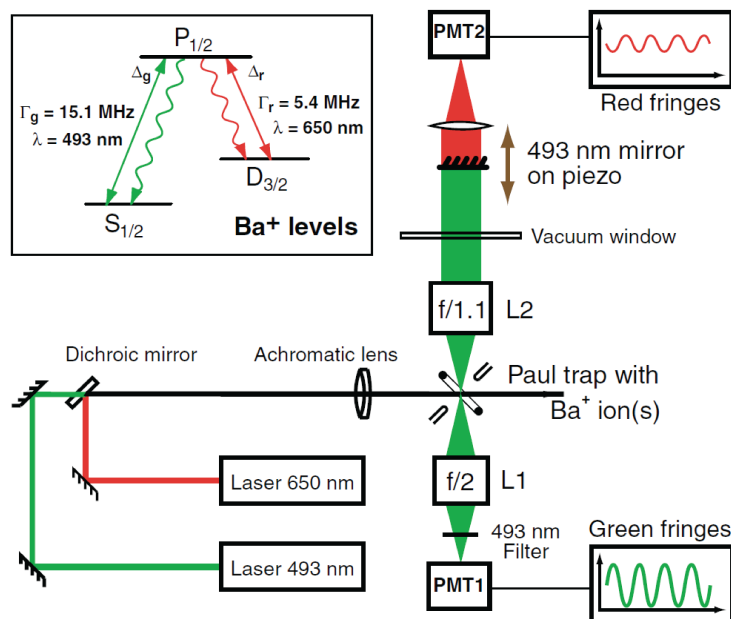


Figure 1.3: Experimental setup and relevant level scheme of Barium for light interference measurements from single atoms and their mirror images [9, 10].

It could be shown, that when the directly emitted and the reflected light field are superimposed at the position of the ion, a back-action on the ion is created by a modification of the electromagnetic vacuum field and the ion's own radiation reaction field. This causes inhibition and enhancement of the ion's spontaneous emission depending

on the mirror position [9]. It also leads to an energy shift of the excited atomic level [10]. This far-field mirror-induced level shift oscillates when the ion-mirror distance is varied. Thus, if the position of the ion is controlled well enough to make it sensitive to this spatial dependence, the level shift can be seen as a spatially varying potential, which gives rise to additional trapping forces[11].

Furthermore such a setup allows continuous readout of the motion and feedback cooling [12].

1.2.2 Towards remote entanglement

A future goal of our project is to obtain remote entanglement between two ions in distant traps. One possible entanglement scheme for this purpose was proposed by Cabrillo et al. [13]. In this scheme two ions with a Λ -shaped atomic level configuration are used. The information is encoded in the ground state $|g\rangle$ or in the (meta)-stable excited state $|e\rangle$ which are both coupled to a common excited state $|a\rangle$ [14]. At the beginning both ions are in the ground state $|g\rangle$ and weakly excited on the $|g\rangle \longleftrightarrow |a\rangle$ transition, so that the probability that both ions are excited at the same time is negligible [13]. When one of the atoms is excited it can spontaneously decay along the $|a\rangle \longleftrightarrow |e\rangle$ transition and the emitted photon is detected. In order to generate an entangled state, the collected photons are mixed on a 50/50 beam splitter to erase the information which path the photon took and therefore making them indistinguishable [14]. If an additional stable phase relation ϕ between the two photon paths is kept, then a photon detection directly projects the atoms onto the $|\Psi\rangle = |ge\rangle + e^{i\phi}|eg\rangle$ Bell state.

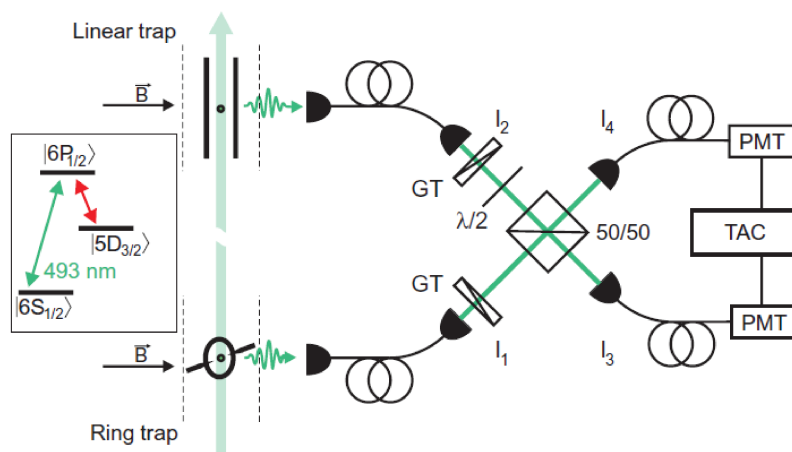


Figure 1.4: Sketch of the experimental setup and the relevant electronic levels of Barium (inset) for the measurement of quantum interference of remotely trapped ions [15]: Resonance fluorescence photons emitted by two remotely trapped ions are overlapped on a 50/50 beam splitter. Subsequently, the second-order correlation is evaluated.

In the past, several experiments have been performed towards remote entanglement. For instance a single-ion two-photon source has been realized, by splitting the reso-

nance fluorescence of a single trapped ion into two parts, delaying one of them and recombining both on a beam splitter. In this way two successively emitted photons may arrive simultaneously at the beam splitter [16].

Another experiment on the way to realize remote entanglement is shown in Fig. 1.4. Two ions are trapped in two remote ion traps of different type. The resonance fluorescence photons emitted by each ion are overlapped on a 50/50 beam splitter. In this way an observation of high contrast interference between resonance fluorescence photons emitted by two remotely trapped ions was realized [15].

The $1.7 \mu\text{m}$ laser will be an important tool for the characterization of the entangled state thus produced.

Chapter 2

Ion motion in a Paul trap

In order to investigate atom-light interactions and QED-effects on isolated particles it is usually necessary to have them stable over long periods of time. To do so, electric, magnetic or optical traps are often used, as they enable to measure their properties with extremely high accuracy. One specific type of trap applicable to ions was invented by Wolfgang Paul, for which he was awarded the Nobel Prize in Physics in 1989. The functioning of this so called “Paul trap” is presented here [17].

2.1 Principle of the Paul trap

Particles can be bound elastically to a coordinate ($\vec{r}_c = 0$) in space if a force, proportional to the distance r away from this coordinate, acts on them [17]. In 3D this would require a parabolic potential

$$\Phi \sim \Phi_0 \sum_i \alpha_i r_i^2 \quad \text{with } i = x, y, z \quad (2.1)$$

which for an ion can be realized with electric quadrupole fields. The coefficients α_i will be related to the trap design.

A consequence of the Maxwell equations is that a charged particle cannot be trapped in three dimensions by static electric fields. The divergence of the electric field in a region with no free charge density equals to zero, so the electrostatic potential Φ satisfies the Laplace equation $\Delta\Phi = 0$ and thus [18]

$$\alpha_x + \alpha_y + \alpha_z = 0. \quad (2.2)$$

From this it is clear that the field must be anti-trapping in at least one direction. Two common potentials fulfill condition (2.2) [17]:

1. A two-dimensional confinement, where

$$\alpha_x = 1 = -\alpha_y, \alpha_z = 0 \quad \text{so that} \quad \Phi = \frac{\Phi_0}{2r_0^2}(x^2 - y^2) \quad (2.3)$$

2. A three-dimensional confinement, where

$$\alpha_x = \alpha_y = 1, \alpha_z = -2 \quad \text{so that} \quad \Phi = \frac{\Phi_0(r^2 - 2z^2)}{r_0^2 + 2z_0^2}$$

with $2z_0^2 = r_0^2$ in cylindrical coordinates

The idea of W. Paul was to then allow confinement in all 3 directions, by applying a periodically time-varying quadrupole potential $\Phi_0 = U_0 + V_0 \cos(\Omega_{RF}t)$ instead of a static one, which on average leads to a resulting force towards the trap center [19].

Although in the Barium laboratory we are operating two trap-types corresponding to the above geometries, a ring trap and a linear trap, in this thesis only the latter will be described since it was the one used for the experiments presented here.

2.2 The linear Paul trap

In the case of a linear trap, a two-dimensional quadrupole potential is applied, which provides confining forces in the two directions perpendicular to the z-axis, while for confinement along the trap axis an additional static axial z potential is added [20].

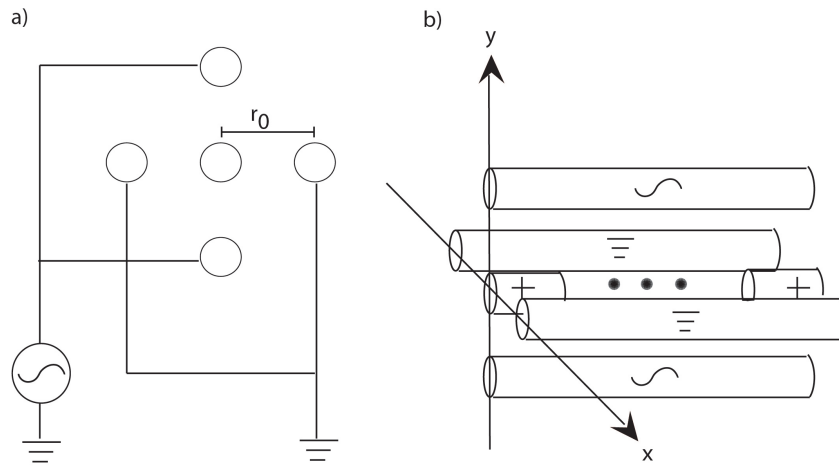


Figure 2.1: Scheme of a linear Paul trap. a) Cross section through the trap center, with the four rods pairwise connected to the diagonally opposite one and the endcap electrode. One pair of rods is grounded while to the other one a RF voltage is applied. b) Side view of the rod- and endcap electrodes with a string of trapped ions. The endcap electrodes are held at a small positive DC voltage to axially confine the ions. [18, 19].

A typical example of a linear trap is shown in Fig. 2.1. Ideally it is composed of two endcap electrodes and four long cylindrical rods. A RF voltage $V(t) = V_0 \cos(\Omega_{RF}t)$ is applied to one diagonal pair of rods, while the other pair is grounded. This configuration provides the required radial trapping potential of Eq. (2.3). Due to the axial symmetry of the design this potential has no z-component and the RF is zero along the trap axis. The axial confinement is generated by the two DC electrodes at either end.

The equations of motion for a particle with mass m and charge Q in this potential are decoupled in the spatial coordinates

$$\ddot{r}_i = -\frac{|Q|}{m} \frac{d\Phi}{dr_i}$$

and take the form of the Mathieu equations [21]

$$\frac{d^2 r_i}{d\tau^2} + (a_i - 2q_i \cos(2\tau)) r_i = 0.$$

a_i , q_i and τ are dimensionless parameters defined as

$$a_i = \frac{4|Q|\alpha_i U_0}{mr_0^2 \Omega_{RF}^2} \quad q_i = \frac{2|Q|\alpha_i V_0}{mr_0^2 \Omega_{RF}^2} \quad \tau = \frac{\Omega_{RF} t}{2},$$

where $2r_0$ is the distance between two diagonal rods.

The parameters a_i and q_i govern the stability of the ion trap. They define the regions in the (a_i, q_i) space where stable solutions of the equations of motion exist. In the lowest order approximation and for the case $(|a_i|, q_i^2) \ll 1$ the stable ion trajectories can be found to be [22]

$$r_i(t) \sim \cos(\omega_i t) \left(1 - \frac{q_i}{2} \cos(\Omega_{RF} t)\right)$$

$$\text{with} \quad \omega_i = \beta_i \frac{\Omega_{RF}}{2} \quad \text{and} \quad \beta_i = \sqrt{a_i + \frac{q_i^2}{2}}.$$

The motion of the trapped ions can be described as a slow (secular) oscillation with frequencies ω_i modulated by a much faster oscillation at the driving frequency Ω_{RF} , namely the micromotion. Micromotion occurs when the oscillating ions depart from the trap axis; then they experience a driven motion in radial direction at the trap frequency. If stray DC fields displace the average ion position from the RF null the ion undergoes excess micromotion [19], but by applying compensating DC-voltages this can be cancelled.

The secular frequency ω_i is a function of the Mathieu parameters a_i and q_i and is therefore mass dependent. In the secular approximation the micromotion is neglected and the secular motion is considered to be generated by a so called harmonic Pseudopotential Ψ [21]

$$Q\Psi = \sum_i \frac{1}{2} m \omega_i^2 r_i^2 \quad i = x, y, z.$$

In the radial direction the secular motion is caused by the RF-potential and ω_i is given by

$$\omega_{x,y} = \beta_{x,y} \frac{\Omega_{RF}}{2} \quad (2.4)$$

whereas in the axial direction the confinement is provided by the endcap DC-voltage U_{cap} so that the harmonic potential takes the form [23]

$$\kappa Q U_{cap} = \frac{1}{2} m \omega_z^2 z_0^2$$

and thus

$$\omega_z = \sqrt{\frac{2\kappa Q U_{cap}}{m z_0^2}}, \quad (2.5)$$

where z_0 is the distance of the endcap electrode from the trap center and κ denotes the field penetration factor.

The depth of the pseudopotential well in the radial and axial directions is given by

$$D_i = \frac{1}{2} m \omega_i^2 r_{i,0}^2 \quad (2.6)$$

where $r_{i,0}$ is the electrode distance from the center of the trap. Typical depths are at the order of a few tens of eV, which makes it possible to load from a thermal beam of atoms [21].

The kinetic energy of the trapped ions can be reduced to the order of $\hbar\omega$ via laser cooling. In this regime the motion of the ion in the harmonic potential has to be quantized using the usual creation and annihilation operators

$$\hat{a}_i^\dagger = \sqrt{\frac{m\omega_i}{2\hbar}} \hat{r}_i + \frac{i}{\sqrt{2m\hbar\omega_i}} \hat{p}_i \quad (2.7)$$

$$\hat{a}_i = \sqrt{\frac{m\omega_i}{2\hbar}} \hat{r}_i - \frac{i}{\sqrt{2m\hbar\omega_i}} \hat{p}_i \quad (2.8)$$

with the position and momentum operators \hat{r}_i and \hat{p}_i . The corresponding Hamiltonian is then given by

$$\hat{H} = \sum_i \hbar\omega_i \left(\hat{a}_i^\dagger \hat{a}_i + \frac{1}{2} \right) = \sum_i \hbar\omega_i \left(\hat{n}_i + \frac{1}{2} \right) \quad (2.9)$$

where \hat{n}_i is the number operator of the oscillation in the harmonic trapping potential, which averaged over a given motional state gives the vibrational quantum number or mean phonon number of the ion [23].

In summary, a trapped ion can be described by the model of a three dimensional quantum harmonic oscillator, oscillating at the respective trap frequencies in each direction. In the next section we want to have a look at what happens when a trapped ion is excited with laser light and how the internal and external degrees of freedom couple to each other.

Chapter 3

Trapped ion coupled to a laser field

The interaction of single trapped ions with laser fields makes it possible to cool them close to their vibrational ground state, by manipulating their internal electronic states and their motion. In the following chapter a description of this light-matter interactions (see Ref. [22] for a review) will be given and the principles of laser cooling are explained. Moreover we discuss how to manipulate and readout the state of the ions via interaction with laser light using the “shelving method”.

3.1 Light-matter interaction

In this section we discuss how the vibrational motion of the ion can be coherently coupled to the internal electronic state using an external laser. For simplicity we consider the interaction of an ion trapped in a harmonic potential with a single laser mode tuned close to the transition of a two level atom with ground state $|g\rangle$ and excited state $|e\rangle$. It is described by the following Hamiltonian [21]

$$\hat{H} = \hat{H}_e + \hat{H}_m + \hat{H}_{int}. \quad (3.1)$$

\hat{H}_e characterizes the internal electronic state of the ion and \hat{H}_m the motion of the ion in the trapping potential as discussed in the preceding chapter. The laser-ion interaction is described by \hat{H}_{int} , where the coupling strength is given by the Rabi frequency Ω [24]. We write

$$\hat{H}_e = \frac{1}{2}\hbar\omega_a\hat{\sigma}_z \quad (3.2)$$

$$\hat{H}_m = \hbar\omega\left(\hat{a}_i^\dagger\hat{a}_i + \frac{1}{2}\right) \quad (3.3)$$

$$\hat{H}_{int} = \frac{1}{2}\hbar\Omega\left(\hat{\sigma}^+ + \hat{\sigma}^-\right)\left(e^{i(\omega_l t - k_l \hat{r})} + e^{-i(\omega_l t - k_l \hat{r})}\right) \quad (3.4)$$

where $\hat{\sigma}_z, \hat{\sigma}^+$ and $\hat{\sigma}^-$ are the Pauli spin matrices and \hat{r} is the operator for the displacement of the ion from its equilibrium position in the trap [21]. ω_a is the atomic transition frequency for $|g\rangle \longleftrightarrow |e\rangle$, ω is the secular trap frequency and ω_l, k_l are

the laser frequency and wave number respectively. By choosing appropriate relations between these three frequencies, efficient coupling between electronic and vibrational degrees of freedom can be obtained.

The interaction Hamiltonian of Eq. (3.4) provides a valid description for electric dipole and quadrupole transitions, as well as for stimulated Raman transitions with the appropriate effective on-resonance Rabi frequencies Ω [22]. The discussion of the atom-light interaction is kept in a general form. The case of the quadrupole transition $|S, m\rangle \longleftrightarrow |D, m'\rangle$, which is of main interest within this thesis, can be obtained by replacing the Rabi frequency in the above expressions by the following term

$$\Omega = \left| \frac{eE_0}{2\hbar} \langle S, m | (\boldsymbol{\epsilon} \cdot \mathbf{r}) (\mathbf{k} \cdot \mathbf{r}) | D, m' \rangle \right|. \quad (3.5)$$

A more detailed consideration of the electric quadrupole transition can be found in the Appendix A.

The ion position operator can be written in terms of creation and annihilation operators (from Eq. (2.7) and Eq. (2.8)) as

$$\hat{r} = \sqrt{\frac{\hbar}{2m\omega}} (\hat{a} + \hat{a}^\dagger).$$

We define the Lamb-Dicke parameter as [21]

$$\eta = k_l \sqrt{\frac{\hbar}{2m\omega}}, \quad (3.6)$$

it describes the coupling of light to the motion of the atom in the ground state. The interaction Hamiltonian then takes the following form

$$\hat{H}_{int} = \frac{1}{2} \hbar \Omega (\hat{\sigma}^+ + \hat{\sigma}^-) \left(e^{i(\omega_l t - \eta(\hat{a} + \hat{a}^\dagger))} + e^{-i(\omega_l t - \eta(\hat{a} + \hat{a}^\dagger))} \right).$$

If we now move into an interaction picture via the unitary transformation $\hat{U} = e^{i(\hat{H}_e + \hat{H}_m)t/\hbar}$, with the interaction Hamiltonian given by $\hat{H}_I = \hat{U}^\dagger \hat{H}_{int} \hat{U}$, this leads to terms of $e^{\pm i(\omega_l \pm \omega_a)t}$. In the rotating wave approximation the two rapidly oscillating terms where ω_l and ω_a add up are neglected, since they hardly affect the time evolution. Thus only the two terms oscillating with frequency $\Delta = \omega_l - \omega_a \ll \omega_a$ are taken into account [22]. This yields the following expression

$$\hat{H}_I = \frac{1}{2} \hbar \Omega \left(\hat{\sigma}^+ e^{-i\Delta t} \exp(i\eta(\hat{a} e^{-i\omega t} + \hat{a}^\dagger e^{i\omega t})) + h.c. \right). \quad (3.7)$$

If we assume that the ion is confined to a spatial region that is significantly smaller than the wavelength of the exciting laser, then the Lamb-Dicke parameter is small [24]. In this so called Lamb-Dicke regime, defined by the condition $\eta^2(2n+1) \ll 1$, where n is the phonon number, we can simplify Eq. (3.7) and expand the interaction Hamiltonian to second order in the Lamb-Dicke approximation

$$\exp\left(i\eta(\hat{a} e^{-i\omega t} + \hat{a}^\dagger e^{i\omega t})\right) = 1 + i\eta(\hat{a} e^{-i\omega t} + \hat{a}^\dagger e^{i\omega t}) + O(\eta^2). \quad (3.8)$$

Inserting this into Eq. (3.7) gives [24]

$$\begin{aligned}
\hat{H}_I &= \frac{1}{2} \hbar \Omega (1 - \eta^2 \hat{a} \hat{a}^\dagger) (\hat{\sigma}^+ e^{-i\Delta t} + \hat{\sigma}^- e^{i\Delta t}) \\
&+ i \frac{\hbar \Omega \eta}{2} (\hat{a} e^{-i\omega t} + \hat{a}^\dagger e^{i\omega t}) \hat{\sigma}^+ e^{-i\Delta t} \\
&- i \frac{\hbar \Omega \eta}{2} (\hat{a} e^{-i\omega t} + \hat{a}^\dagger e^{i\omega t}) \hat{\sigma}^- e^{i\Delta t} \\
&- \frac{\hbar \Omega \eta^2}{4} (\hat{a}^2 e^{-2i\omega t} + (\hat{a}^\dagger)^2 e^{2i\omega t}) (\hat{\sigma}^+ e^{-i\Delta t} + \hat{\sigma}^- e^{i\Delta t}). \tag{3.9}
\end{aligned}$$

This means, that as the ion oscillates in the trap, in its rest frame the phase of the laser field is modulated at the trap frequency, which leads to sidebands in the absorption spectrum. Thus the laser can couple the state $|g, n\rangle$, where n is the vibrational quantum number, to all states $|e, n'\rangle$. Absorption or emission processes can occur on sidebands of the electronic transition, so that the energy difference $\hbar\Delta$ is transferred in kinetic energy of the ion and the phonon number n is changed [21].

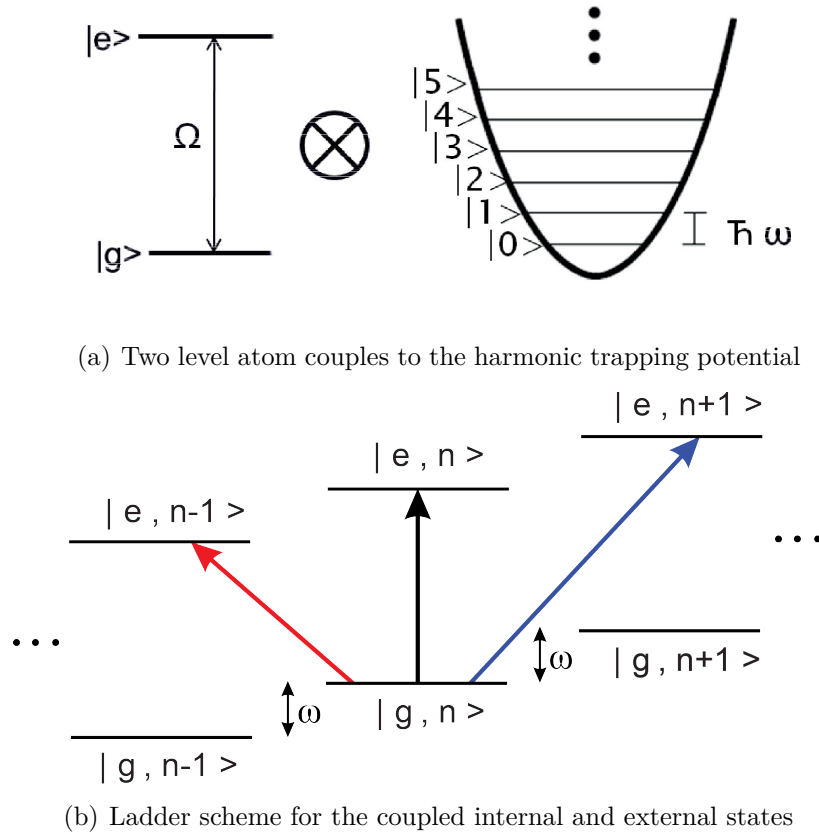


Figure 3.1: Due to the excitation with an external laser field the vibrational motion of the ion can be coherently coupled to the internal electronic state. This leads to the energy level diagram shown above with carrier, first red sideband and first blue sideband excitations [24, 25].

By setting the laser detuning Δ near the resonance of a specific transition, only one time-independent expression remains in Eq. (3.9), whereas the other terms oscillate at frequencies that are multiples of ω [26]. Neglecting these off resonant terms leads to the ladder scheme illustrated in Fig. 3.1 where we can identify carrier and sideband transitions. When the laser frequency is tuned to resonance $\Delta = 0$ the carrier transition $|g, n\rangle \longleftrightarrow |e, n\rangle$ is excited and the interaction Hamiltonian reduces to [24]

$$\hat{H}_{carrier} = \frac{1}{2}\hbar\Omega_{n,n}(\hat{\sigma}^+ + \hat{\sigma}^-) \quad (3.10)$$

with coupling strength

$$\Omega_{n,n} = \Omega(1 - \eta^2 n). \quad (3.11)$$

If the laser is detuned below the carrier frequency by one unit of the trap frequency $\omega_l = \omega_{atom} - \omega$ the first red sideband is excited and the Hamiltonian takes the form [24, 25]

$$\hat{H}_{red} = \frac{1}{2}i\hbar\Omega_{n,n-1}(\hat{a}\hat{\sigma}^+ - \hat{a}^\dagger\hat{\sigma}^-) \quad \text{with} \quad \Omega_{n,n-1} = \eta\sqrt{n}\Omega. \quad (3.12)$$

This interaction removes one quantum of secular motion while the internal electronic state is excited. In other words, the Hamiltonian gives rise to transitions of the type $|g, n\rangle \longleftrightarrow |e, n-1\rangle$, which entangle the motional state with the internal state of the ion. It is equivalent to the Jaynes-Cummings Hamiltonian in quantum optics, except that it involves the absorption of a trap phonon instead of one laser photon [22].

If the laser is blue detuned by one unit of the trap frequency, the first blue sideband is excited respectively [24]

$$\hat{H}_{blue} = \frac{1}{2}i\hbar\Omega_{n,n+1}(\hat{a}^\dagger\hat{\sigma}^+ - \hat{a}\hat{\sigma}^-) \quad \text{with} \quad \Omega_{n,n+1} = \eta\sqrt{n+1}\Omega. \quad (3.13)$$

This Hamiltonian will drive transitions like $|g, n\rangle \longleftrightarrow |e, n+1\rangle$ and is sometimes referred to as anti-Jaynes-Cummings Hamiltonian. It describes an excitation process, where one trap phonon is emitted when the atom goes to the excited state. This Hamiltonian is usually neglected in the Jaynes-Cummings model.

3.1.1 Time evolution and Rabi flopping

When the laser is tuned close to resonance, $\Delta = m\omega + \delta$ where $\delta \ll \omega$, of the transition $|g, n\rangle \longleftrightarrow |e, n+m\rangle$, coupling to other levels can be neglected given that the laser intensity is sufficiently low $\Omega_{n,n+m} \ll \omega$ for all $n, n+m$ [21]. If this is the case, then the ion's dynamic behavior is governed by the few resonant terms of Eq. (3.9) and the time evolution of the general state [22]

$$|\Psi(t)\rangle = \sum_n c_{g,n}(t)|g, n\rangle + d_{e,n}(t)|e, n\rangle \quad (3.14)$$

is determined by the time-dependent Schrödinger equation with the interaction Hamiltonian before the Lamb-Dicke approximation, given by Eq. (3.7) [22]. Inserting the

general state $|\Psi(t)\rangle$ into the Schrödinger equation leads to the set of coupled equations [21]

$$\dot{c}_{g,n} = -i^{(1-|m|)} e^{i(\delta t - \phi)} (\Omega_{n+m,n}/2) d_{e,n+m} \quad (3.15)$$

$$\dot{d}_{e,n+m} = -i^{(1+|m|)} e^{-i(\delta t - \phi)} (\Omega_{n+m,n}/2) c_{g,n}. \quad (3.16)$$

The Rabi frequency $\Omega_{n+m,n}$ denotes the coupling strength between the state $|n\rangle$ and $|n+m\rangle$ and is defined by [21]

$$\Omega_{n+m,n} := \Omega \langle n+m | \exp(i\eta(\hat{a}e^{-i\omega t} + \hat{a}^\dagger e^{i\omega t})) | n \rangle. \quad (3.17)$$

This set of coupled differential equations can be solved by the method of Laplace transforms, for a detailed discussion see Ref. [22] and Ref. [21].

In the case of on-resonant excitation ($\delta = 0$) the solution takes the following form

$$\begin{pmatrix} c_{g,n}(t) \\ d_{e,n+m}(t) \end{pmatrix} = \begin{pmatrix} \cos(\Omega_{n+m,n}t/2) & -ie^{i\frac{\pi}{2}|m|} \sin(\Omega_{n+m,n}t/2) \\ -ie^{-i\frac{\pi}{2}|m|} \sin(\Omega_{n+m,n}t/2) & \cos(\Omega_{n+m,n}t/2) \end{pmatrix} \begin{pmatrix} c_{g,n}(0) \\ d_{e,n+m}(0) \end{pmatrix}.$$

The solutions show sinusoidal exchange of population between the states $|g, n\rangle$ and $|e, n+m\rangle$ caused by a sequence of stimulated absorption and emission processes, so called Rabi flopping. If $m \neq 0$ it describes the on resonant excitation of sideband transitions of m -th order. In the case of on resonant carrier excitation $m=0$ the matrix describes the periodic population exchange between ground and excited state of the ion. Given that at time $t=0$ the population was in the ground state, then after resonant carrier excitation for the so called π -time $\Omega t = \pi$ the population is completely transferred to the excited state. For resonant sideband excitation the same periodic oscillations can be observed, but with a different frequency. In the case of off-resonant excitations $\delta \neq 0$ the population is not transferred completely and therefore the oscillation contrast decreases while the oscillation frequency increases.

3.1.2 State detection via electron shelving

The internal state of the ion can be detected by laser-induced fluorescence on a short-lived cycling transition as indicated in Fig. 3.2. This can be achieved by an additional level $|a\rangle$ coupled by a strong probe laser to the ground state $|g\rangle$. The photons scattered on this transition can then be detected with photomultipliers or charge-coupled-device (CCD) cameras. This signal not only allows the detection of the ion itself, but makes it also possible to distinguish between the internal states of the ion by the so called electron shelving method [27, 28]. For this method the three level system $|g\rangle$, $|e\rangle$ and $|a\rangle$ is used, where the transitions $|g\rangle \longleftrightarrow |e\rangle$ and $|g\rangle \longleftrightarrow |a\rangle$ can be driven independently by laser fields.

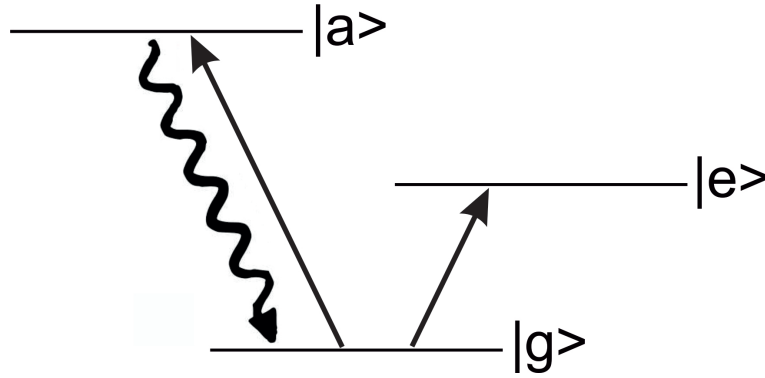


Figure 3.2: Fluorescence readout of the atomic state via electron shelving: The $|g\rangle \longleftrightarrow |e\rangle$ transition and the $|g\rangle \longleftrightarrow |a\rangle$ cycling transition can be driven independently by laser fields. Due to photon-scattering on the $|g\rangle \longleftrightarrow |a\rangle$ transition the ion is either projected in the ground or excited state. If the ion is in the ground state, many photons are scattered on the cycling transition. In the excited state the probe laser is off resonant and no scattered photons can be detected, the ion remains dark [24].

If the ion is projected into $|g\rangle$ by the first scattering event, many photons can be detected [22]. Whereas if the ion is in the excited state $|e\rangle$, it is not resonant with the probe laser and no photons are scattered. By repeating this measurement several times it is possible to determine the excitation probability of the metastable excited state $|e\rangle$.

The lifetimes of the $|g\rangle \longleftrightarrow |a\rangle$ transition needs to be much shorter than the one of the $|g\rangle \longleftrightarrow |e\rangle$ transition, in order to distinguish between the count rates for excited and ground state. This is the case if electronic quadrupole and dipole transitions are used. In our setup $|g\rangle \longleftrightarrow |e\rangle$ corresponds to the electronic quadrupole transition $|S_{1/2}\rangle \longleftrightarrow |D_{5/2}\rangle$ and $|g\rangle \longleftrightarrow |a\rangle$ is realized using the dipole transition $|S_{1/2}\rangle \longleftrightarrow |P_{1/2}\rangle$.

The electron shelving method is for example used to measure Rabi oscillations, where the excited state probability is detected as a function of the laser pulse duration coupling the ground and excited state. Spectroscopy is another application of this technique. There the excited state probability is measured as a function of the frequency of the coupling laser, which leads to a full spectrum of the investigated transition as will be shown later in this thesis.

3.2 Laser cooling

To investigate the quantum mechanical properties of the ion-trap system it is necessary to reduce the kinetic energy of the ion to a few $\hbar\omega$, where ω is the trap frequency. Very effective tools for this purpose are laser cooling techniques (see Ref. [22] for a review), such as Doppler or sideband cooling [29, 30, 31], which work with near resonant excitation of an atomic transition. We discuss here how combining these two mechanisms can provide cooling of thermal ions near the quantum mechanical ground state.

3.2.1 Doppler cooling

The ion will be considered here as a two level system, moving with velocity v in a trap with frequency ω . If ω is much lower than the decay rate Γ of the cooling transition, then one cycle of photon absorption and emission can occur faster than changes of the velocity v due to the confining potential. If a traveling wave laser field, with frequency ω_l , Rabi frequency Ω and detuning $\Delta = \omega_l - \omega_a$ from the atomic resonance, is applied to the ion, it can be treated like a free particle seeing a time-dependent Doppler-shifted laser frequency [21].

If the laser beam is detuned below the electronic transition the probability to absorb a photon will be higher if the ion is moving towards the laser beam due to the Doppler effect, than for an ion moving in beam-direction. Stimulated absorption, as well as stimulated and spontaneous emission processes can take place. If the ion absorbs a photon with wave vector k it undergoes a change of momentum $\Delta p = \hbar k$ in the wave vector direction of the light field, whereas the emission will be homogeneously distributed in all directions [7]. Thus emission will lead to a zero net average momentum transfer, and to a random walk, similar to Brownian motion. The rate of absorption-emission cycles depends on the excited-state probability ρ_{ee} and on the decay rate Γ , therefore the average radiation pressure force acting on the ion is given by [22]

$$\left(\frac{dp}{dt}\right)_a \sim F_a = \hbar k \Gamma \rho_{ee} \quad (3.18)$$

and leads to an effective cooling of the ion, up to the so called Doppler cooling limit defined by

$$T_{min} = \frac{\hbar\Gamma}{2k_B}. \quad (3.19)$$

A more detailed discussion of the Doppler cooling limitations can be found in the Appendix B.

3.2.2 Sideband cooling

In the regime where the decay rate from the excited state Γ is lower than the motional frequency ω the individual motional sidebands become resolved. This is the requirement for coherent manipulation of the internal and motional states, as well as for cooling to the ground state. After an initial Doppler cooling stage to the Lamb-Dicke regime and with no other heating mechanisms present, sideband cooling to the ground state of motion is possible [22].

An ion excited to the state $|e\rangle$ can spontaneously decay to the ground state $|g\rangle$ and from there be excited again. If the laser is tuned to the first red sideband, as shown in Fig.3.3, these cycles of excitation and emission processes remove one phonon per cycle and consequently cool the atom beyond the Doppler limit [24].

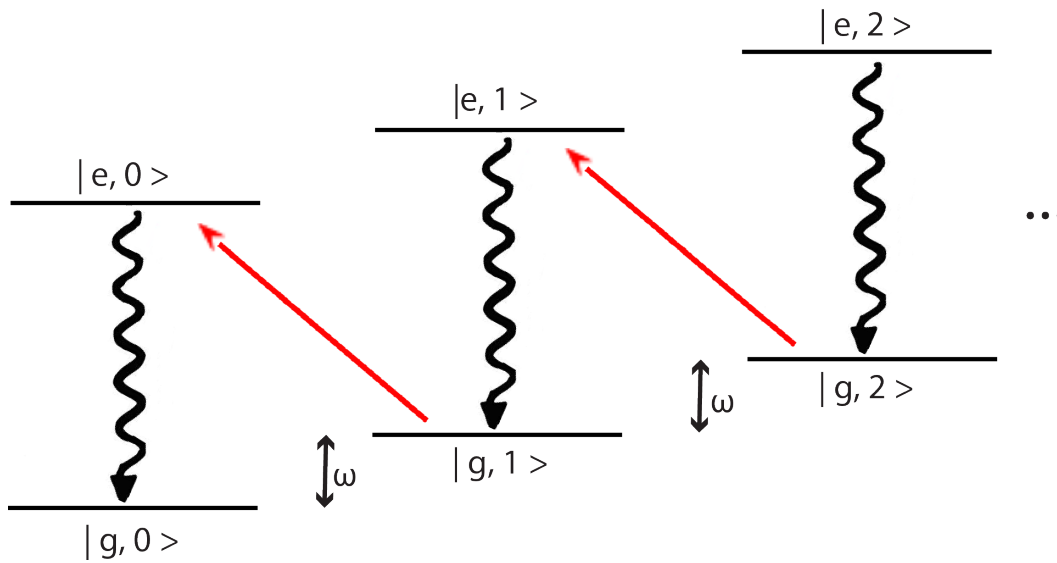


Figure 3.3: Sideband cooling scheme: Transition from the ground state $|g, n\rangle$ to the excited state $|e, n - 1\rangle$ on the red sideband followed by a spontaneous decay on the carrier leads to the state $|g, n - 1\rangle$. Iteratively this sequence allows for cooling to the motional ground state [25].

The cooling rate R_n for the state $|n\rangle$ depends on the excited-state occupation probability $P_e(n)$, its decay rate Γ and the Rabi frequency on the red sideband given by Eq. (3.12) [22]

$$R_n = P_e(n)\Gamma = \Gamma \frac{(\eta\sqrt{n}\Omega)^2}{2(\eta\sqrt{n}\Omega)^2 + \Gamma^2} \quad (3.20)$$

and vanishes once the ground state is reached. This would imply that the ground state is a dark state of the red sideband excitation, but this is prevented by off-resonant excitation of the carrier and first blue-sideband. Both heating processes occur with a probability proportional to Ω^2 . For the final stage of cooling $\langle n \rangle \ll 1$ the problem can be restricted to the ground ($n=0$) and first excited ($n=1$) states with the corresponding occupation probabilities. The final mean excitation number $\langle n \rangle$ after resolved sideband cooling can be estimated by comparing the probabilities of ending up in the excited

state $|e\rangle$ after exciting the ion on the red and blue sideband. The ratio of these probabilities is given by [22]

$$R = \frac{p_e^{rsb}}{p_e^{bsb}} = \frac{\langle n \rangle}{(\langle n \rangle + 1)} \quad (3.21)$$

and thus the mean occupation number of the thermal motional state takes the form

$$\langle n \rangle = \frac{R}{1 - R}. \quad (3.22)$$

Chapter 4

Experimental setup

In this chapter the experimental apparatus relevant for the measurements performed within this thesis is presented. After a general overview of the setup, a detailed account of the individual parts is given.

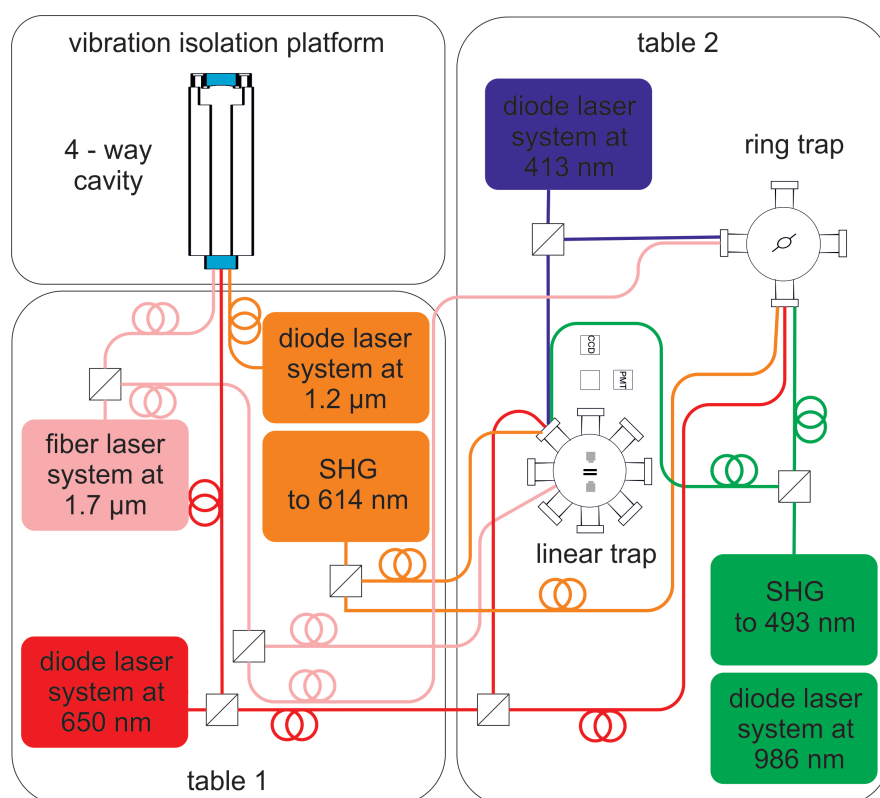


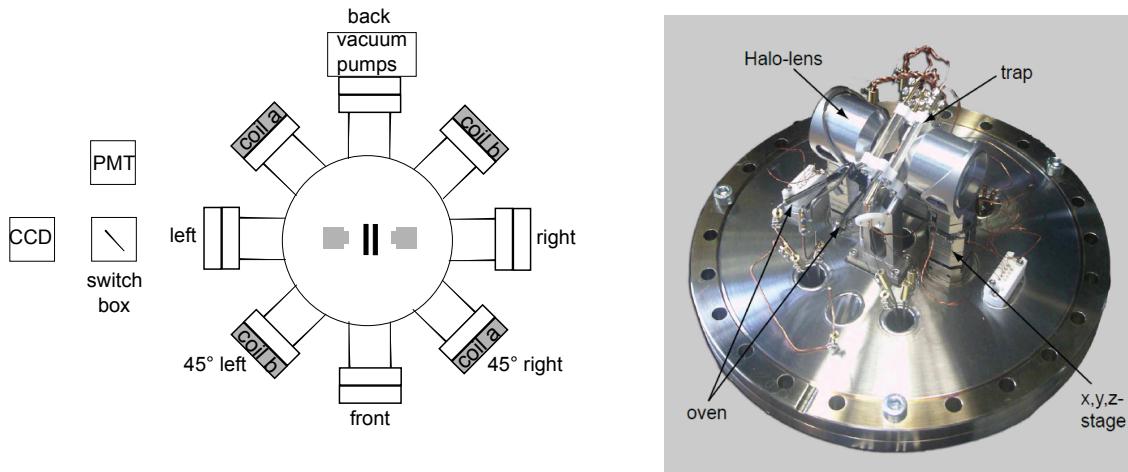
Figure 4.1: Overview of the experimental apparatus. The experiment is spread over two optical tables and one vibration isolated platform. Two diode lasers, one at 650 nm and one frequency doubled from 1.2 μm , and a fiber laser at 1.7 μm together with their stabilization, are located on table 1. The diode lasers at 413nm and 986 nm, with its frequency doubling to 493nm, and the vacuum vessel containing the linear Paul trap are on the other table. The cavities for locking the 650 nm, 1.2 μm and 1.7 μm lasers are located on the vibration isolation platform.

The apparatus consists of two main components, the vacuum vessel with the trap setup and the laser systems. The vacuum setup with the linear Paul trap and the setups for the lasers at 413 nm, 493 nm and 650 nm are briefly described, while the main part is dedicated to the 1.2 μm and 1.7 μm laser systems. One section is also dedicated to the intensity stabilization for the 1.7 μm laser and the principles of feedback control.

4.1 Vacuum vessel and linear trap setup

In this section the most important parts of the vacuum and trap setup are explained. For a more detailed discussion see [23, 32].

In order to enable investigations of the properties of single trapped Barium ions it is necessary to avoid collisions with background gases and to achieve low heating rates. Therefore the trap needs to be situated in an ultra high vacuum (UHV). This is provided by placing the trap into an octagon steel vacuum vessel, which is held at a pressure of about 10^{-11} mbar with an ion-getter-pump. A titanium-sublimation pump is used periodically to remove residual gas in the chamber. A vacuum gauge allows the measurement of the pressure inside the chamber.



(a) Top view of the vacuum vessel and linear Paul trap setup

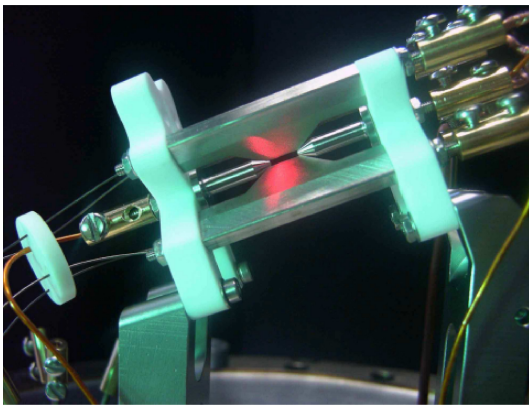
(b) Experimental flange with Barium ovens, HALO lenses and linear trap [23]

Figure 4.2: (a) Top view of the octagonal vacuum vessel showing the 8 CF-63 ports. 7 are equipped with fused-silica view ports and one is connected to an ion-getter-pump and a titanium-sublimation-pump to maintain the UHV. Two pairs of Helmholtz coils (a and b) generate a constant magnetic field at the ion position. Two HALO lenses and the linear Paul trap are situated in the center of the vessel. The state detection of the ion can either be realized by detecting the scattered laser light on a PMT or a CCD camera. (b) Photograph of the main flange with the two Barium ovens, the linear Paul trap and the two HALO lenses positionable by piezo translation stages [23].

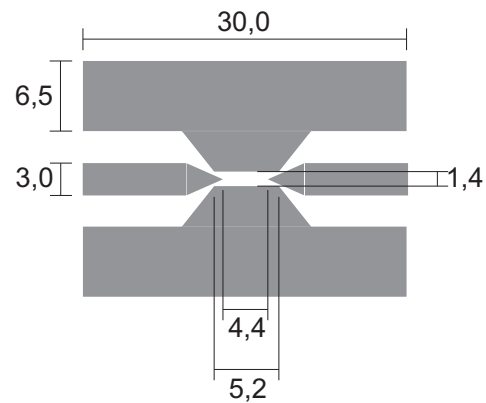
The vessel is equipped with 8 CF-63 ports in the horizontal plane and 2 CF-200 ports at the top and the bottom of the vessel. The vacuum pumps and a vacuum valve are attached to the one CF-63 port in the back. Two Barium ovens, two HALO-lenses and

the linear trap are placed on a large CF-200 flange, as shown in Fig. 4.2(b), which is mounted upside down to the top port of the vessel.

The magnetic field at the position of the ion is generated by three pairs of Helmholtz coils hosted around the CF-63 and CF-200 ports respectively. Two of them are situated in the horizontal plane (see Fig. 4.2(a) coil pairs a and b) and allow for a deliberate orientation of the magnetic field in this plane, while the third one is mounted in the vertical plane and compensates for the earth's magnetic field. The “left” and “right” view ports in Fig. 4.2(a) are the observation channels and the magnetic field is orientated parallel to this observation axis. To guarantee a good optical access for laser manipulation and measurements on the ion, the other 7 CF-63 ports and the bottom CF-200 port are equipped with fused-silica view ports, with anti-reflection coating for the wavelengths at 493 nm, 650 nm and $1.7 \mu\text{m}$. For further optical access two HALO (high aperture laser objectives) lenses with a numerical aperture of 0.4 are positioned at a distance of 14 mm from the ion.



(a) Photograph of the linear trap illuminated with a laser pointer [23].



(b) Side view-scheme and dimensions of the trap in mm.

Figure 4.3: Linear Paul trap with dimensions

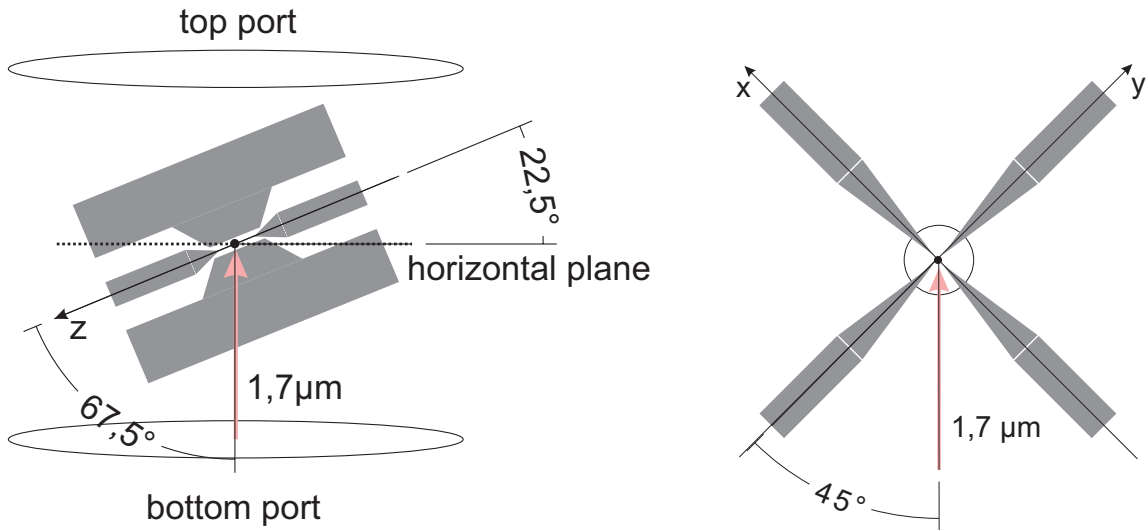
The linear Paul trap consists of four blade-shaped and two tip electrodes. The quadrupole potential is generated by applying a high power radiofrequency to two opposite blades, while the other pair is grounded. The high RF power is achieved using a helical resonator. The axial confinement is obtained by connecting the two tips to a DC voltage. Additional pairs of DC electrodes can be used to compensate for micromotion, such electrodes are realized by thin wires as shown in Fig. 4.3(a).

The trap dimensions are shown in Fig. 4.3(b). The distance from the trap center to the RF-electrodes is given by $r_0 = 0.7 \text{ mm}$ and to the DC-electrodes it is $z_0 = 2.2 \text{ mm}$ respectively. With a tip voltage of $U_{cap} = 2000 \text{ V}$ and a field penetration factor $\kappa = 0.075$, the axial trap frequency can thus be estimated using Eq. (2.5) from Sec. 2.2. The driving radio-frequency of $\Omega_{RF}/2\pi = 15.1 \text{ MHz}$ with an amplitude of $V_0 = 1225 \text{ V}$ and an offset $U_0 = 0 \text{ V}$ leads, according to Eq. (2.4) from Sec. 2.2, to the following

trapping parameters

$$\begin{aligned} a_{x,y} &= 0 \\ q_{x,y} &\cong 0.48 \\ \frac{\omega_{rad}}{2\pi} &= \frac{\omega_{x,y}}{2\pi} \cong 1.96 MHz \\ \frac{\omega_z}{2\pi} &\cong 1.05 MHz \end{aligned}$$

The “main” laser cooling directions are from the front port or from the 45° left port, see Fig. 4.2(a). The trap is tilted by an angle of 22.5° from the horizontal plane of the vacuum vessel to ensure projections of the cooling laser onto all the oscillation directions of the ion.



(a) Tilt of the trap with respect to the horizontal plane of the vacuum vessel and angle between the 1.7 μm laser and the trap axis z.

(b) Front view of the trap and angle between 1.7 μm laser and the trap axes x and y.

Figure 4.4: Trap geometry and angle between incident 1.7 μm laser and the individual trap axes.

With the given trap parameters and the angle φ between the laser beam direction \vec{k} and the oscillation axis one can also calculate the Lamb-Dicke parameter η . In the case of the 1.7 μm laser the angle between the laser and the radial direction is $\varphi = 45^\circ$ and for the axial direction it is $\varphi = 67.5^\circ$ as shown in Fig. 4.4.

$$\begin{aligned} \eta_{rad,z} &= \cos \varphi k \sqrt{\frac{\hbar}{2m\omega_{rad,z}}} \\ \eta_{rad} &\cong 0.011 \\ \eta_z &\cong 0.008 \end{aligned}$$

Due to the high mass of Barium and the not optimally chosen angles the Lamb-Dicke parameters are very small. Therefore the Lamb-Dicke regime given by $\eta^2(2n + 1) \ll 1$

is easily obtained after Doppler cooling. On the other hand this results in a weak coupling strength for excitations on the sidebands and therefore decreases the efficiency for sideband cooling.

4.2 Laser systems

In this section a brief description of the laser systems at 413 nm, 493 nm and 650 nm is given, more information regarding this setup can be found in [33, 34, 23]. Since it is the first time that the 1.2 μm and the 1.7 μm laser systems are used in the group, they will be presented in more detail.

Photo-ionization laser at 413 nm

Loading of ions in the trap is realized by sending a neutral beam of atoms through the trap center, where they are ionized with a laser-diode system from Toptica (DL100) at a wavelength of 413 nm via a 2 step photo-ionization. The beam of neutral atoms emerges from two stainless steel tubes filled with Barium grains heated by sending a current of 4 A through them. The light provided by the laser system is sent to the trap with an intensity of around 2 mW. The wavelength is measured with a wavemeter¹ and adjusted respectively.

The photo-ionization itself occurs by a two-photon process. The ion is first excited from the 1S_0 to the 3D_1 state and then with the second absorbed photon it is ionized [23].

Doppler cooling, state detection and prepumping laser at 493 nm

The laser field at a wavelength of 493 nm is generated by frequency doubling the light of a commercially available diode laser (Toptica DL pro 986) with an output power of 130 mW at 986 nm. The master laser is locked to a reference cavity with a Finesse $F \approx 1000$ and stabilized by the Pound-Drever-Hall technique [35] (see Sec.5.3). A small fraction of the light is sent to a wavemeter¹, so that the wavelength can be constantly monitored. The second harmonic is generated by pumping a KNbO_3 crystal at the focus of a bow-tie cavity with the 986 nm light. After being frequency shifted by ~ 500 MHz by an AOM in a double pass configuration the resulting 493 nm output is locked to a tellurium vapor cell (Te_2) using Doppler free modulation transfer spectroscopy (MTS, see [36]). The output power of the second harmonic generation is ~ 30 mW and the generated wavelength can be tuned towards the ion's resonance by changing the driving frequency of a double pass AOM by ± 30 MHz. Then the light is split for Doppler cooling and prepumping. Both beams are frequency shifted by AOMs before being sent to the trap. The prepumping laser is shifted for ~ 140 MHz to be close to resonance with the atomic transition, whereas the cooling laser is shifted for ~ 116 MHz, so that it is detuned about 20 to 40 MHz below the atomic resonance. Both laser beams can be pulsed by switching the RF-signal that is driving the AOMs. The functioning of this laser pulsing is explained more detailed in SubSec. 4.3. The light is then sent to the trap, by single-mode polarization maintaining fibers.

The 493 nm laser light, exciting the $|S_{1/2}\rangle \longleftrightarrow |P_{1/2}\rangle$ transition, is used for Doppler cooling, state preparation and detection.

¹ HighFinesse GmbH, Laser and Electronic Systems, Wavelength Meter WS7

Repumping laser at 650 nm

The light field at the wavelength of 650 nm is provided directly by a commercially available diode laser system (Toptica DL 100) in Littrow configuration with an output power of 10 mW. A part of the light is sent via a polarization maintaining fiber to the four way cavity described in Chap. 5 for frequency stabilization. The remaining power is sent to the second optical table via a single-mode, polarization maintaining fiber, where part of it is led to a wavemeter¹ and the wavelength can be continuously monitored. The other part is coupled into an additional fiber and guided to the trap. The wavelength can be detuned by changing the driving frequency of a double pass AOM configuration, which can be controlled with the lab computer.

The 650 nm laser is used to repump the ion from the $|D_{3/2}\rangle$ to the $|P_{1/2}\rangle$ state, from where it spontaneously decays into the electronic ground state.

4.2.1 Frequency doubled 1.2 μm repumping laser

The laser at the wavelength of 1.2 μm is a commercially available diode laser system (Toptica DL 100). In this subsection the functioning of a diode laser will briefly be discussed. Then the optical setup of the 1.2 μm laser and the frequency doubling² to a wavelength of 614 nm is described.

Diode laser functioning and frequency doubling

Diode lasers are electrically pumped semiconductor lasers. The most common type is realized by a p-n junction or a p-i-n structure, in which the gain is generated by an electrical current flowing through. This leads to the recombination of electrons and holes, releasing the energy portions as photons. With optical feedback in a laser resonator, this effect can be stimulated by incident photons, leading to optical amplification and to laser oscillation.

In our setup the master laser is realized by an external-cavity laser diode³, where the resonator consists of the diodes rear facet and a holographic grating. The beam emitted from the diode is collimated by an antireflection coated lens and stabilized by a Littrow configuration. Thus the beam is led to a dispersive optical holographic grating, where the first order is sent back into the laser diode to control its frequency. By simultaneously changing the angle between laser beam and grating surface and changing the length of the resonator, a mode hop free frequency tuning is possible over several GHz⁴. The master oscillator is lasing at a wavelength of 1228.3 nm with a maximum output power of 25 mW.

² Toptica Photonics TA/DL-SHG 110 Frequency Doubled High Power Laser System

³ LD-1230-0030-DFB-1

⁴ Toptica Photonics TA/DL-SHG 110 Manual

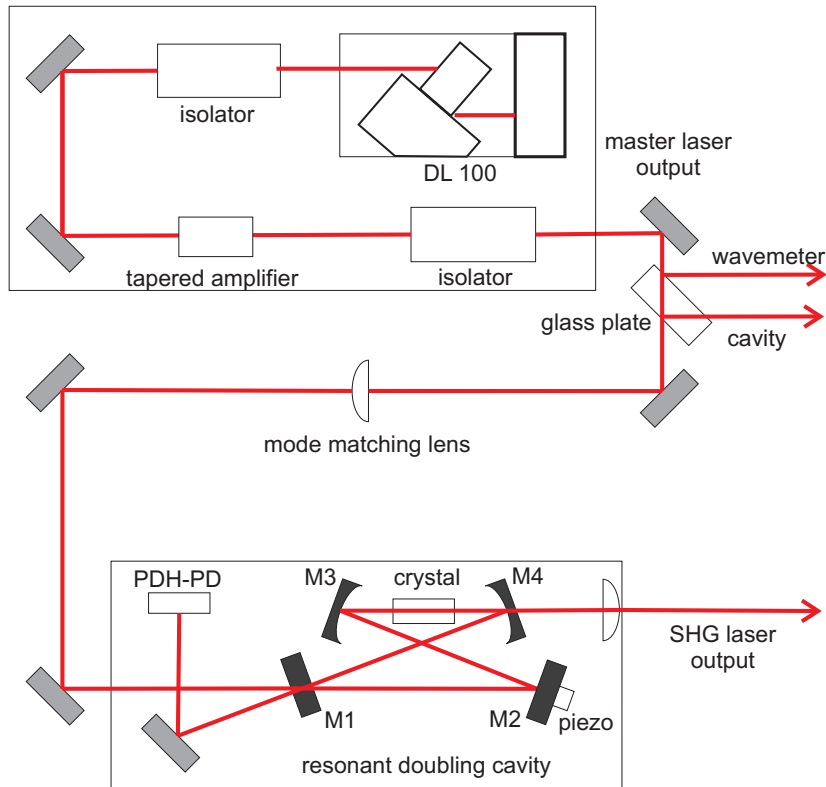


Figure 4.5: Schematic of the frequency doubling $1.2 \mu\text{m}$ laser system⁴. See text for details.

The fundamental laser light passes through an optical isolator, to avoid feedback of laser radiation into the diode laser, and is amplified by a laser diode with tapered gain region. After passing through another isolator, a glass plate is inserted in the beam path to generate two probe beams of $2 \times 0.5 \text{ mW}$, used for measuring the wavelength and for frequency stabilization. Then the master laser is mode matched to the fundamental mode of the resonant doubling cavity. There the second harmonic laser light is generated by a frequency doubling KNbO_3 crystal mounted inside a bow-tie ring resonator. The ring resonator (see Fig. 4.5) is composed of two plane (M1, M2) and two concave mirrors (M3, M4). The infrared pump light is partially transmitted by M1, its transmittance is optimized to achieve the highest intensity in the ring cavity. M2 is mounted onto a piezo element, which is driven by the error signal generated by the electronic cavity length stabilization unit, and allows to adjust the cavity length. The wavelength of the output beam is 614.17 nm and we achieve an output power of $>2 \text{ mW}$.

Optical setup

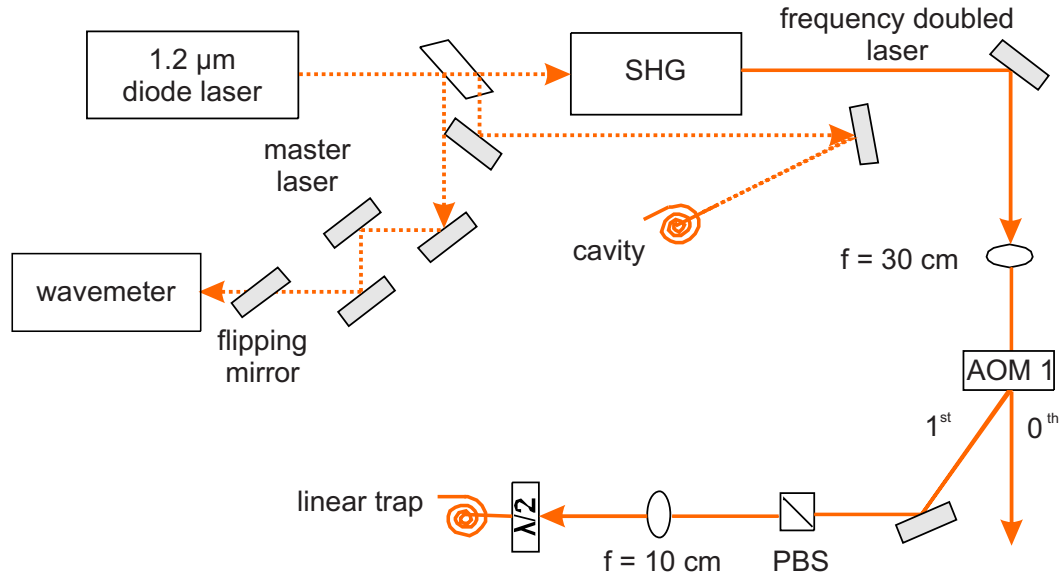


Figure 4.6: Optical setup of the $1.2 \mu\text{m}$ laser system: The laser diode emits light at $1.2 \mu\text{m}$. Parts of the master beam (dashed line) are sent to a wavemeter and to a reference cavity for PDH-frequency stabilization. The remaining light is frequency doubled (continuous line) to 614 nm by a second harmonic generation (SHG) stage and frequency shifted for 180 MHz with a single pass AOM configuration. The resulting beam is sent to the trap by a single-mode polarization maintaining fiber.

After emission from the laser diode the light is sent through a glass plate to the frequency doubling unit. At the two surfaces of the glass plate a part of the master laser is reflected. The first reflected beam is sent to a wavemeter⁵, while the second is sent to the reference cavity for frequency stabilization of the laser by the Pound-Drever-Hall technique [35] (see Sec. 5.3). The SHG beam is frequency shifted of 180 MHz with an AOM⁶ in single pass configuration. This AOM can either be continuously diffracting or switched on and off by the lab computer in order to generate pulsed laser sequences, the generation of these sequences is explained more detailed in SubSec. 4.3. Finally the laser beam is coupled into a single-mode polarization maintaining fiber and led to the trap with a laser power of $50\text{-}100 \mu\text{W}$.

The laser at the wavelength of 614 nm is used to repump the ion from the long lived $|D_{5/2}\rangle$ state back into the faster decaying $|P_{3/2}\rangle$ state.

⁵ Bristol Instruments Model 621 Laser Wavelength Meter

⁶ Crystal Technology Inc. Model 3200-121

4.2.2 Laser for the quadrupole transition at 1.7 μm

The laser at the wavelength of 1.7 μm is a commercially available fiber laser system (Koheras Adjustik^{TM7}). After discussing the general functioning of a fiber laser, in this subsection the optical setup of the 1.7 μm laser is described. Subsequently we characterize the properties of the laser system.

Fiber laser functioning

In a fiber laser, optical fibers are used as a gain medium. Usually these fibers are doped with rare earth ions and pumped by laser diodes. In our case a distributed feedback fiber laser (DFB laser) is used, where the active region is periodically structured as a diffraction grating.

For laser operation in the range between 1720-2000 nm, as it is the case in our setup, a thulium (Tm^{3+}) doped fiber can be used. The laser is a DFB fiber laser, with a 5 cm long DFB Bragg grating directly in the thulium doped fiber, which acts as a distributed reflector. The fiber laser is core-pumped by a 1600 nm diode and the output is amplified using a master oscillator power amplifier (MOPA) configuration. This means, that the DFB master laser is followed by another thulium doped fiber to amplify the output power. By cooling the substrate on which the fiber is placed with Peltier elements, the cavity length and therefore also the laser wavelength can be changed. This allows a thermal tuning of the wavelength over a range of 1109 pm in steps of 36.9 pm/K. To improve the frequency stability provided by the thermal control, a piezo electric wavelength tuning over a range of 31 pm is implemented. This allows frequency locking of the laser to an external reference cavity (see Chap. 5). The laser is protected from back-reflections by an optical isolator and angled connectors are used for the output fiber. The vacuum-wavelength is specified to be 1762 nm at a maximum output power of 70 mW with a single mode suppression ratio of >25 dB ⁸

⁷ NKT Photonics Koheras AdjustikTM Turn-Key System RTAdT20PztS

⁸ Koheras AdjustikTM Turn-Key System Manual

Optical setup

In standard configuration we operate the laser system at a temperature of 43.6 °C and at maximum output power of ca. 70 mW.

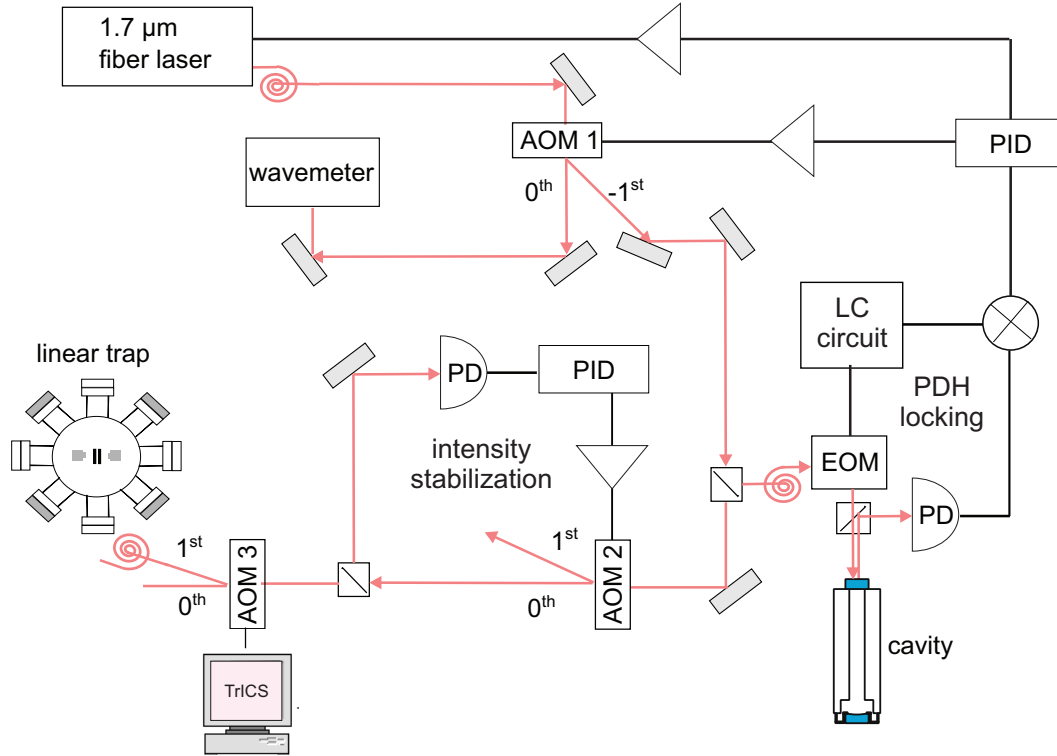


Figure 4.7: Optical setup of the 1.7 μm laser system: The emitted laser light passes through an AOM1. The 0^{th} order is detected on a wavemeter. The frequency shifted -1^{st} order is partially used for frequency stabilization and part of it is sent to the ion after being intensity stabilized and frequency shifted by another AOM3. See text for details.

The laser light is fiber guided to the optical table, where it is sent through a Faraday isolator to avoid feedback of laser radiation into the laser. After passing through an AOM (AOM1⁹) the 0^{th} order of the beam is sent to the wavemeter¹⁰. The -1^{st} order is frequency shifted by about -250 MHz and split into two parts by a polarizing beam splitter (PBS). One of these two beams is fiber guided to the reference cavity for frequency stabilization (see Chap. 5), while the other one is sent to another AOM (AOM2¹¹) for intensity stabilization. A small fraction of the light is guided to a photodiode for intensity stabilization, whereas the rest is sent through a third AOM (AOM3¹¹) and frequency shifted for +250 MHz. AOM3 is connected to the Pulse box and the 1^{st} order can be switched by the lab computer to generate laser pulses (see SubSec. 4.3). Then the light is sent through a single-mode polarization maintaining fiber to the trap, where we obtain a laser power of ca. 5 mW.

⁹ Brimrose 410-472-7070 mod. IPF-250 40-F

¹⁰ Bristol Instruments Model 621 Laser Wavelength Meter

¹¹ Brimrose 410-472-7070 mod. IPF-250 40-F

4.3 Generating experimental sequences

In order to do spectroscopy or observe Rabi oscillations we need to generate laser pulse sequences. These experimental sequences originate from a programmable pulse generator (PPG), which was developed by Philipp Schindler. In this section a brief description of the pulse sequence generation is given, a detailed description can be found in Philipp's diploma thesis [37].

Asynchronous analog and digital control voltages are controlled via a National Instruments PCI card, whereas the programmable pulse generator is used to generate synchronous exactly timed digital (TTL) and radio frequency (RF) pulses.

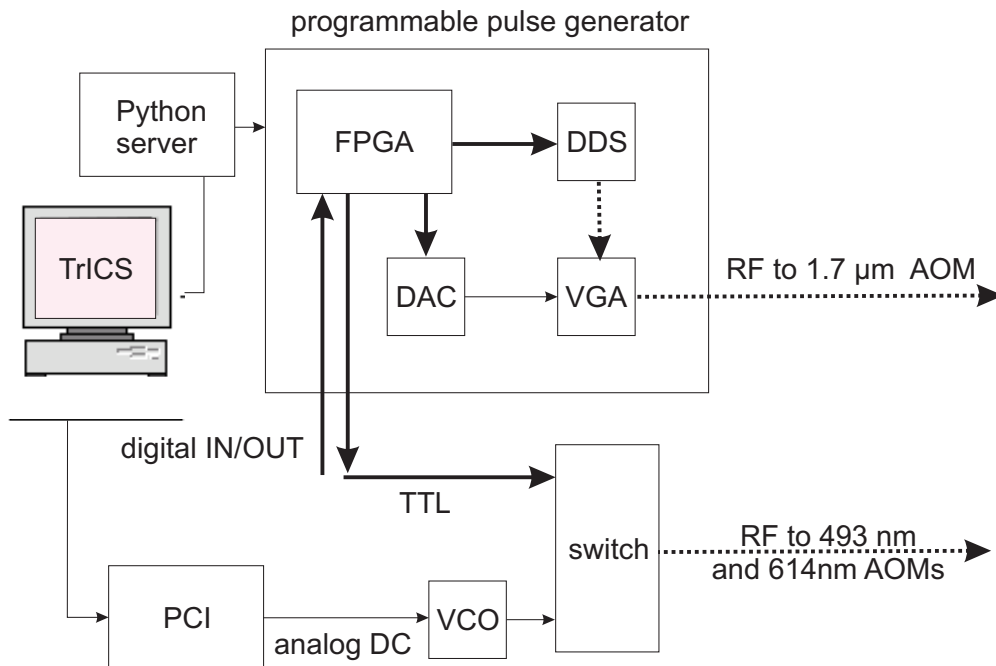


Figure 4.8: Schematic setup of the computer controlled programmable pulse generator. Generation and switching of the radio frequency signals driving the AOMs for generating laser sequences [37].

The centerpiece of the programmable pulse generator is a complex logic chip, a so called field programmable gate array (FPGA). It is an integrated circuit and contains logic blocks that can be configured to perform complex combinational functions. The FPGA configuration is specified by using a hardware description language. Given that the FPGA has only digital outputs, a direct digital synthesizer (DDS) is needed to generate radio frequency pulses. A DDS is a type of frequency synthesizer, which creates arbitrary waveforms from a frequency reference clock. It offers a better control over the generated radio frequency signal, than analog techniques as for example VCOs. Therefore switching between frequencies or switching on and off the RF-signal can be achieved in a few hundred nanoseconds. Furthermore it allows for phase coherent switching between several frequencies within a few microseconds, if the phase is controlled digitally and switched with great accuracy. Amplitude modulated radio frequency pulses can be realized with a digital to analog converter (DAC) combined

with a variable gain amplifier (VGA), controlled by the digital outputs of the FPGA. It is possible to control up to 16 DDS and DAC with an FPGA, if additional addressing electronics are implemented.

For the 493 nm and 614 nm lasers the pulses are realized by switching the radio frequency signal driving the respective AOMs. This is done by commercial switches¹² driven by a voltage controlled oscillator¹³, controlled by the PCI card and a TTL signal, generated by the FPGA. The generated output signal is amplified by an RF-amplifier and then applied to the AOM. For the 614 nm laser we use a POS box with integrated VCO¹⁴, but due to non satisfying switching of this box we inserted an additional second switching of the same kind as described above. In the case of the 1.7 μm laser the radiofrequency signal driving the AOM (AOM3) is directly generated by the DDS board.

The whole system can be controlled with the lab computer. For this purpose we use a multi-platform software program called TrICS (written in c and c++), which was specifically developed by Thomas Holleis, in collaboration with Florian Zähringer. It allows direct observation of the ions count rate on the user interface and to set the frequencies for the cooling, the prepumping and the repumping laser. Depending on the desired sequence a short program is written in the Python open source programming language and can then be executed by loading it in TrICS, from where it is sent to the Python server. The human readable sequence is converted into machine code and sent to the FPGA. On the TrICS user interface one can choose how often the sequence should be running, how many measurements are done per datapoint and with what resolution the measurement is to be taken. An example for such a Python program used for generating laser pulse sequences is given in the Appendix E.

¹² Mini-Circuits Switch ZASWA-2-50DR+ DC-5GHz

¹³ Mini Circuit VCO ZX95-200-S+ 100-200 MHZ

¹⁴ Mini-Circuits Plug-In Voltage Controlled Oscillator POS-200

4.4 Intensity stabilization of the 1.7 μm laser

In order to have good control over the ions state a constant laser intensity is required. Therefore measurements characterizing the laser intensity have been performed, revealing intensity fluctuations on the order of 10% and an amplitude modulation peak at 80 MHz. To reduce the observed power fluctuations a feedback control loop is used for intensity stabilizing the laser. The experimental realization and the obtained results are presented in the following section, after giving a general introduction to the principle of feedback control.

4.4.1 Characterization of the laser intensity fluctuations

Our observation of the laser intensity fluctuations showed a large single frequency amplitude modulation at 80 MHz which contains 10-50 % of the over all laser power. It is not clear what the reason for this peak is and because the company does not reveal detailed information about the internal structure of the laser and possible sources of this noise we do not really know where it is coming from. Therefore we performed several measurements to characterize the peak, so that we might get a hint about its origin.

We observed, that the power in the peak is dependent on the polarization settings and can be minimized to about 10 % of the over all laser power. This was measured by sending the laser light through a $\lambda/2$ waveplate and a polarizing beam splitter to a fast photodiode and detecting the resulting DC signal modulated at 80 MHz. Then the polarization settings where changed so that the DC signal is as high as possible while the ratio between 80 MHz noise and DC background is minimized. Next in this configuration we also tried to measure to what degree the laser is polarized, by trying to cancel out the DC part of the signal by changing the position of the waveplate, so that only the 80 MHz noise remains. But we have not been able to cancel out the DC background by changing the polarization only. This could lead to two different conclusions, either our laser is an incoherent mixture of two polarizations, or the remaining DC signal results from higher order peaks as for example 160 MHz, which cannot be detected by the photodiode anymore and therefore contributes to the DC signal.

We also investigated the dependence of the frequency position of the 80 MHz peak on the laser power, it is shown in Fig. 4.9.

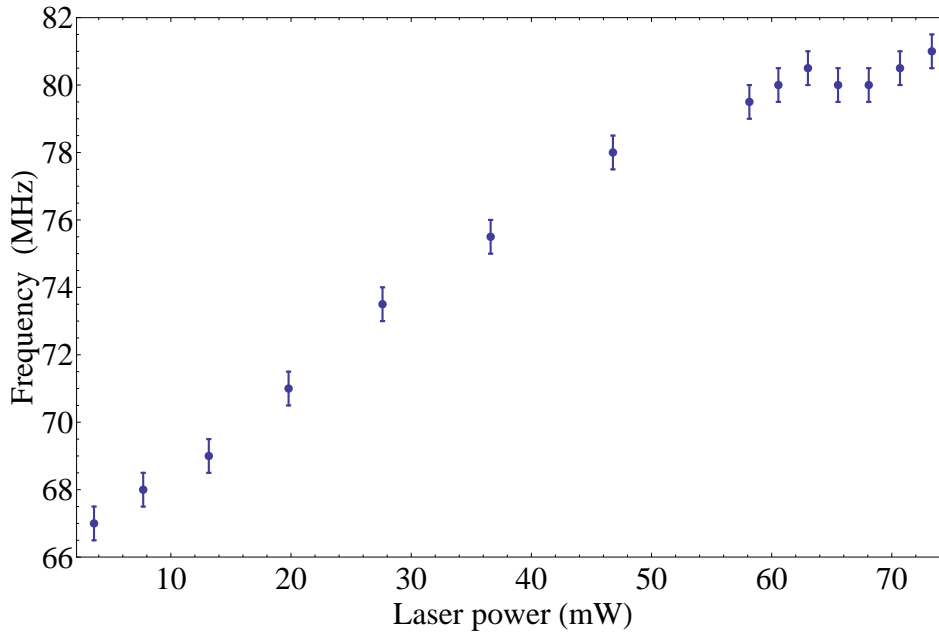


Figure 4.9: Dependence of the position of the 80 MHz peak on the laser power.

As can be seen in Fig. 4.9 the frequency position of the noise is linearly depending on the laser power.

In addition to this 80 MHz peak we observe amplitude fluctuations up to 10 %. These variations mostly occur on timescales of seconds. Due to the dependence of the Rabi frequency on the laser intensity these fluctuations limit the reliability of coherent excitations of atomic transitions. Therefore a stabilization that reduces this slow variation was implemented, the principle of such a feedback control and the experimental setup (see Fig. 4.11) are discussed more in detail in the following subsections.

Measurements have shown that these slow fluctuations depend on the position of the laser piezo and also on the polarization settings.

4.4.2 Basic principle of feedback control

Control theory is used to analyze the behavior of dynamical systems. Based on observations of the system the control loop automatically intervenes to create or conserve desired conditions. Different realizations for control loops are possible, the following description focuses on control via a closed feedback loop, like it was used in the experiment. Only an overview of the basic principles is given, a more detailed discussion of the topic can be found in [38, 39, 40].

The most elementary feedback control setup consists of the system which needs to be controlled, characterized by its complex transfer function $G(s)$, a sensor to measure its output and a controller $K(s)$. The goal is to make the system's output $Y(s)$ faithfully follow a reference signal $R(s)$ by compensating for all the disturbances $D(s)$ acting on the system. In order to realize this, the controller compares the output with the reference signal and according to the difference $E(s)$ generates the system's input $U(s)$. In Fig. 4.10 a block diagram of such a control system is shown [38, 40].

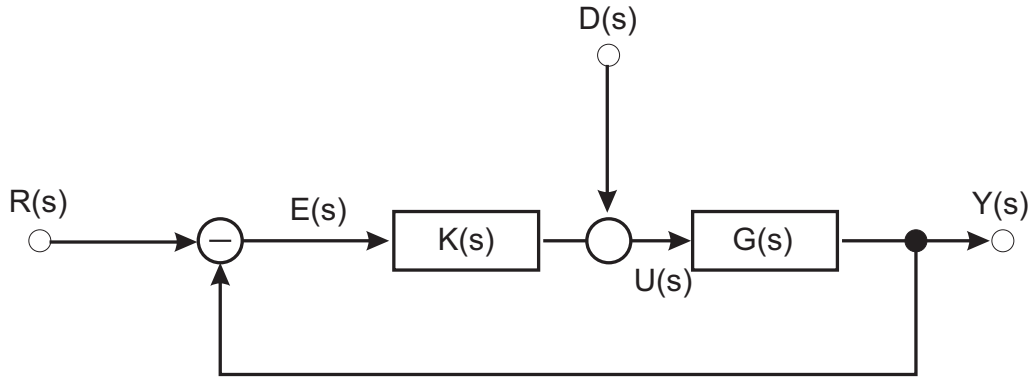


Figure 4.10: Block diagram illustrating the feedback control of a system $G(s)$ with disturbances $D(s)$ by a controller $K(s)$ [38, 40].

For the system shown in 4.10 and described above its sensibility to perturbations (see appendix C for details) is given by

$$S(s) = \frac{1}{1 + K(s)G(s)}$$

and it becomes clear that it gets less sensitive with higher values of $K(s)$. Therefore one would be tempted to increase $K(s)$ as much as possible to achieve fast and efficient cancelation of disturbances. However in the case of higher order systems this is not the case, there phase changes of more than π are possible and the negative feedback can turn into positive feedback. In the case $K(s)G(s) = -1$ the denominator can even become zero and the system will get unstable and oscillate at its resonance frequency $s = i \omega_{res}$ [41].

The most important requirements a control loop has to fulfill are that the system should follow changes of the set value as fast as possible (command tracking) over a frequency range as big as possible, disturbances should be well suppressed (regulation) and the closed loop behavior should be stable within the frequency range (stability). Different types of controllers can be used for stabilization in order to match this requirements. Here only the proportional (P) and the integral (I) controller are discussed, as well as their combination the PI-controller which was used in the setup.

The P-controller amplifies the deviation $e(t)$ from the set value by the factor K_p and transmits the resulting signal $y(t) = K_p e(t)$ without time delay. The feedback loop is stable and damped for all values of K_p , but for a finite gain the long-term response to a steady-state input differs from the desired setpoint [38]. The I-controller performs a summation of the deviation $e(t)$ over a certain time and multiplies the result with a factor K_i , the resulting signal is given by $y(t) = K_i \int_0^t e(\tau) d\tau$. The integral will build up as long as $e(t) \neq 0$ and eliminates the steady state error. The I-controller loop is slower than other feedback control loops, but it has the advantage that it regulates to the desired setpoint [38].

The PI-controller is a combination of proportional and integral controller, which gives faster response while still eliminating steady-state errors. The resulting signal for the PI-controller is given by $y(t) = K_p e(t) + K_i \int_0^t e(\tau) d\tau$ and its transfer function is given by $K(s) = K_p + \frac{K_i}{s}$ respectively [38].

In order to guarantee command tracking, regulation and stability the control parameters need to be tuned to optimum. Many different methods are available to optimize a

control loop. One of the most common experimentally used algorithms is the Ziegler-Nichols method [42], named after its developers. It is a heuristic method based on an experiment on the control circuit and it can only be used, if the control loop does not get harmed when the stability boundary is reached [41]. The principle is to only use the proportional part of the controller in first place and to increase the proportional gain until the closed loop gets unstable and performs continuous oscillations. By means of this critical gain K_k and the oscillation period T_k , the parameters of the integrational part (and if desired also of an additional derivative part) can then be chosen according to the Ziegler-Nichols rule of thumb:

control type	K_p	K_i	T
P	$0.5 \times K_k$	-	-
PI	$0.45 \times K_k$	$1.2 \times \frac{K_p}{T_k}$	$0.85 \times T_k$

Table 4.1: Settings of the control gain according to the Ziegler-Nichols method [40].

4.4.3 Experimental realization and results

The output power of the 1.7 μm laser amplitude shows fluctuations up to 10 %. These variations affect the effectiveness of coherent excitations on atomic transitions due to the dependence of the Rabi frequency on the laser intensity. Therefore an intensity stabilization was implemented, the setup is shown in Fig. 4.11.

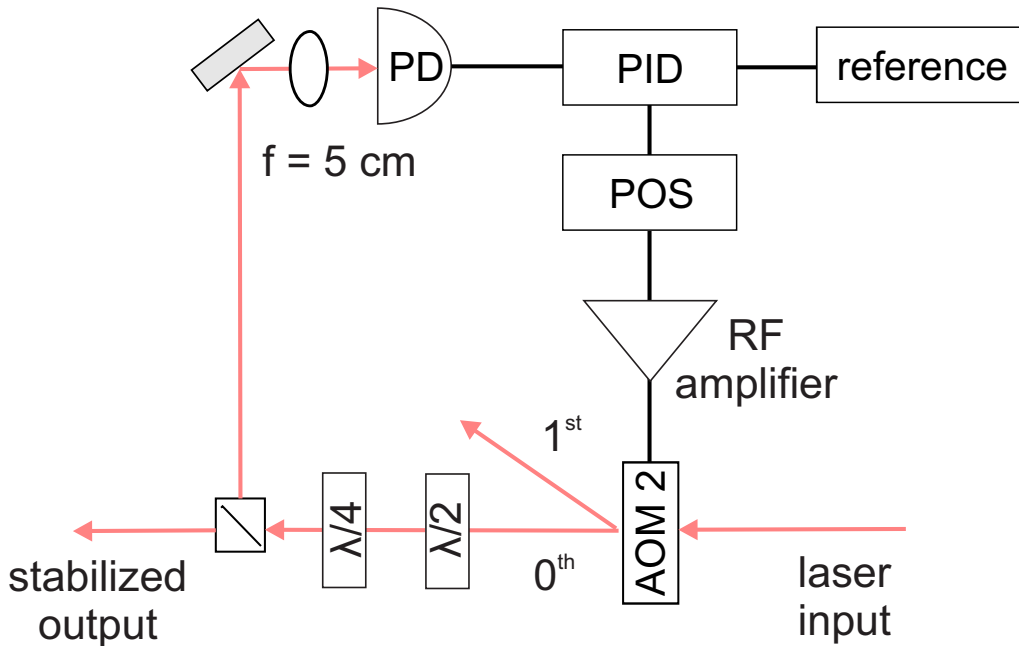


Figure 4.11: Schematic setup of the intensity stabilization for the 1.7 μm laser. The 0th order signal of AOM2 is detected on a photodiode and sent to a PI-controller. There it is compared to the set value defined by the reference. The resulting error signal is fed back to the RF-amplifier driving AOM2. See text for details.

An acousto-optic modulator (AOM 2) is inserted in the optical path of the 1.7 μm laser

for intensity stabilization. A small fraction of the 0^{th} order is branched off and sent to a photodiode¹⁵, in order to detect fluctuations in the laser intensity. A PI-controller¹⁶ compares the incoming PD signal to the set value and generates a corresponding error signal. The output signal of the PI-controller is fed back to the amplitude input of the RF-amplifier that is driving AOM 2. Therefore the RF output power is modulated according to the generated errorsignal and thus the feedback compensates for fluctuations by increasing or decreasing the diffraction efficiency of the AOM and sending more or less power into the first order beam. In order to counteract power drops or increases of 10 %, the setpoint was chosen at around 90 % of the laser power before the AOM. Fig. 4.12 shows a comparison of the resulting intensity noise spectrum with stabilization to the one without stabilization.

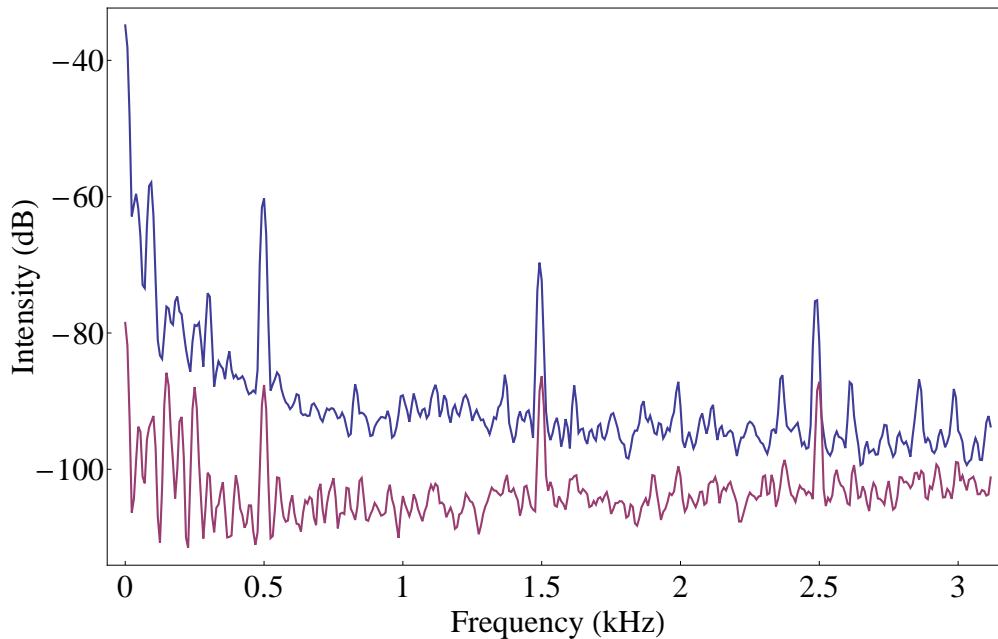


Figure 4.12: Intensity noise spectrum up to 3 kHz with (violet trace) and without (blue trace) intensity stabilization.

As shown in Fig. 4.12 by intensity stabilizing the system, fluctuations at frequencies below 3 kHz can be reduced by 10-20 dB. A measurement of the power variations over longer timescales has also been performed, an example is shown in Fig. 4.13. In this case the fluctuations can be reduced to 2 %.

¹⁵ Thorlabs, PDA 10D

¹⁶ PI-controller with Sample and Hold function, Version 3.0, 2009 designed by Gerhard Hendl

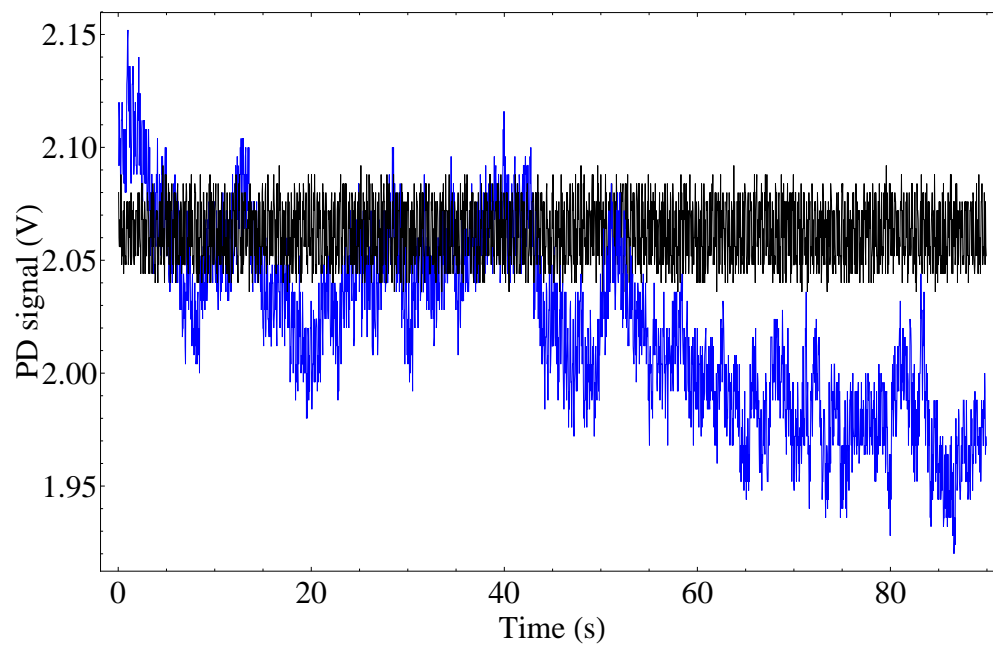


Figure 4.13: Intensity fluctuations on timescales of minutes with (black trace) and without (blue trace) intensity stabilization.

Chapter 5

Locking of the 1.7 μm laser to a high finesse cavity

In this chapter a detailed description of the 4 way reference cavity for the frequency stabilization of the 1.7 μm , the 1.2 μm and the 650 nm lasers is given. The cavity used in the experiment was custom-made based on Jan Benhelm's [43] design, which was further developed and adjusted by Muir Kumph. After describing the design and the setup, the cavity of the 1.7 μm laser is characterized. At the end of the chapter the locking of the 1.7 μm laser to the cavity by the Pound-Drever-Hall technique is explained.

5.1 Cavity design and setup

A laser can be stabilized by locking it to a reference cavity. For this purpose we use 4 Fabry-Perot type resonators, all built up of one flat and one concave mirror positioned on a spacer at a distance $L = 100$ mm. The spacer and the mirrors are made out of ultra-low expansion glass (ULE®), which has a thermal expansion coefficient of less than $10^{-8}/\text{K}$ [44]. In the case of the dipole lasers the flat mirrors are glued on the spacer and the concave mirrors are mounted on it with two concentric piezo transducers. With this setup, thermal drifts can be largely suppressed and it allows tuning the cavity over several free spectral ranges ($\text{FSR} = 1.5$ GHz) by changing the voltage applied to the piezo electrodes. [43]. For the quadrupole laser the cavity length cannot be changed by a piezo, because the thermal expansion coefficient of the piezo is much bigger (on the order of $10^{-6}/\text{K}$) than the one of the ULE and it would make it less precise over long timescales.

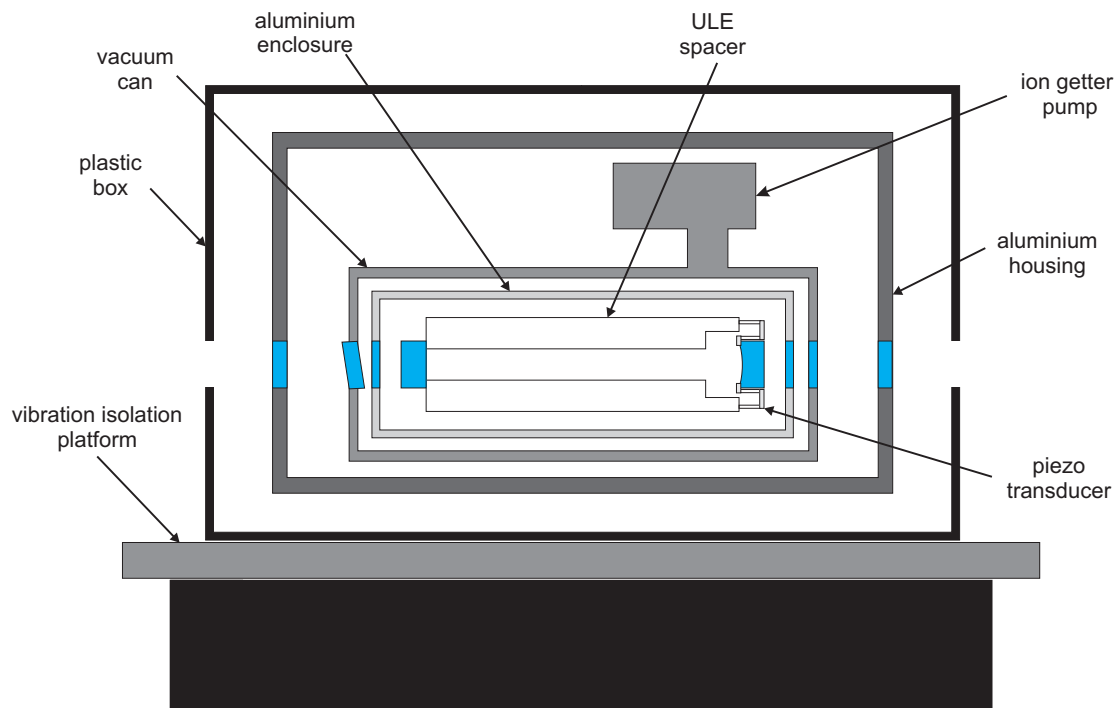
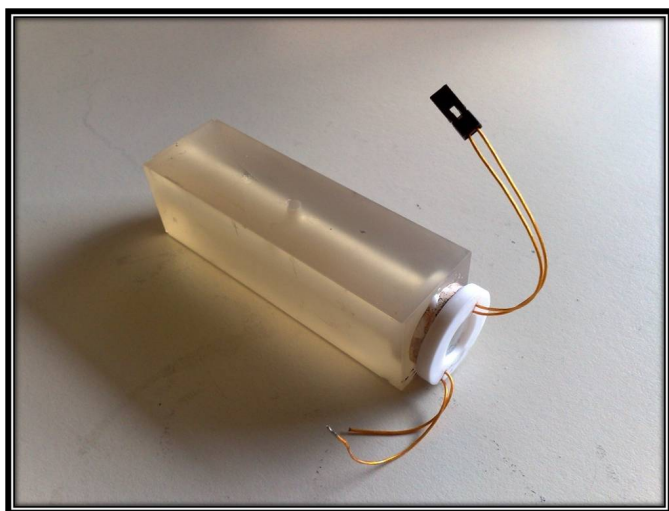


Figure 5.1: Cavity setup to frequency stabilize the $1.7 \mu\text{m}$, $1.2 \mu\text{m}$ and 650 nm lasers. A flat and a curved mirror are kept at a distance of 100 mm by a ULE spacer. For the $1.2 \mu\text{m}$ and 650 nm laser the curved mirror can be tuned by piezo transducers, while for the $1.7 \mu\text{m}$ laser the mirror distance is fixed. The 4 resonators are placed in a vacuum chamber at a pressure of 10^{-6} bar . It is surrounded by a metal housing, a layer of polystyrene and a plastic housing [43]. See text for details.



(a) Cavity spacer made of ultra low expansion glass (ULE) and piezos



(b) Front view of the cavity with vacuum housing

Figure 5.2: Photographs of the cavity spacer and vacuum housing

For the stability of the reference it is important to reduce its sensibility to external perturbations as for example changes of air pressure or temperature, as well as acoustic

noise or seismic vibrations. For this reason the cavity is surrounded by an aluminium enclosure and placed in a stainless steel vacuum can. The vacuum chamber is kept at a constant pressure of 10^{-6} bar with an ion getter pump. This provides a good thermal isolation from the environment and prevents pressure changes. The windows of the vacuum can are anti-reflection coated and the input port is slightly tilted. For further thermal stabilization the vacuum can is enclosed in another aluminium housing with windows specifically coated for the required wavelengths. For temperature stabilization 4 Peltier elements are connected to the metal box. The temperature can be controlled and monitored with a temperature controller¹ connected to the lab computer². The metal housing is surrounded by a 5 cm thick layer of polystyrene for acoustic isolation. Finally the entire setup is enclosed by a plastic box. To avoid vibrational disturbances the cavity setup is mounted on a vibration isolation platform³.

¹ Communicating thermo electric temperature controller, ibrt scientific and engineering solutions, TEC V2.11 (c) 2005

² see www.ibrt.es.com/products/tecmanual2006.html for more details

³ Minus-K Technology 150BM-1

5.2 Characterization of the cavity for the 1.7 μm laser

5.2.1 Cavity parameters

An optical cavity can in principle be characterized by its free spectral range FSR and its finesse \mathcal{F} . The FSR is defined as the frequency difference between two identical spatial modes, for example the distance between two neighboring TEM₀₀ modes. It is given by the inverse round trip time of the light inside the cavity. For a cavity consisting of two highly reflecting mirrors at a distance L we thus have

$$FSR = \frac{c}{2L}. \quad (5.1)$$

With our cavity dimensions L= 10 cm the calculations lead to a free spectral range of FSR = 1.5 GHz.

The other important cavity parameter is the finesse \mathcal{F} , it is directly related to the resonator losses and gives a measure of the power that is left in the resonator after one roundtrip without additional incoming power. It depends on the reflectivity R , transmission T and losses A of the mirrors according to the following relations

$$\mathcal{F} = \frac{\pi\sqrt{R}}{1-R} = \frac{\pi\sqrt{1-A-T}}{A+T} \quad (5.2)$$

with $R + T + A = 1$, and gives a measure of the photon storage time in the cavity. The finesse can be measured by a so called cavity ring-down measurement, where the decay time τ of the light leaking out of the cavity is determined. The finesse is then given by

$$\mathcal{F} = \frac{c\pi\tau}{L} = 2\pi\tau FSR. \quad (5.3)$$

For the ring-down measurement the laser is tuned to resonance, so that the cavity is filled with light and a part of it is transmitted. At time $t = 0$ s the laser was switched off very fast and the exponential decay of the transmitted 1.7 μm laser intensity was observed with a fast photodiode on an oscilloscope. The result of such a cavity ring-down measurement is shown in Fig. 5.3.

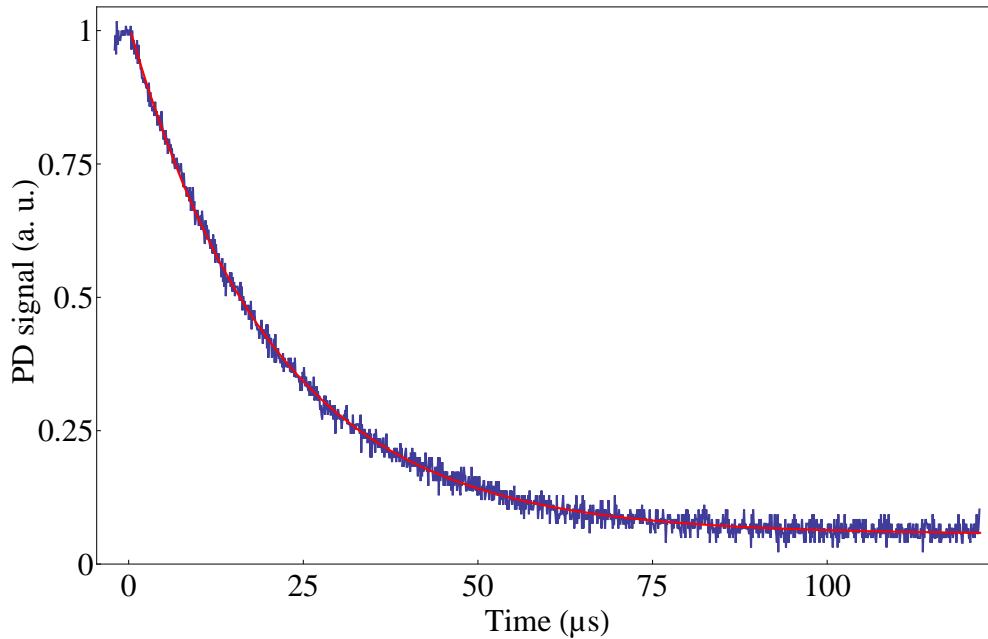


Figure 5.3: Ring-down measurement for determination of the cavity finesse. The decay of the light intensity is measured as a function of time and then fitted by an exponential decay. In this case a decay time τ of $20.7(3) \mu\text{s}$ was measured.

A crucial point of this measurement is the fast switching. By a separate measurement of the switching time we could ensure that the switching is done much faster than the decay time is. Eight data sets were taken and fitted with an exponential decay function to determine the decay time. This leads to a mean decay time of

$$\tau = (20.6 \pm 0.3) \mu\text{s} \quad (5.4)$$

and thus to a finesse of

$$\mathcal{F} = 193600 \pm 2400. \quad (5.5)$$

The quoted reflectivity for the cavity mirrors⁴ at 1.7 μm was $R > 99.98\%$. Inserting this lower bound into Eq. (5.2) would lead to a finesse of about 15700 which is more than a factor 10 lower than the measured one. This means that the actual mirror reflectivity is very well within specifications. The cavity linewidth $\delta\nu$ is the full width at half maximum (FWHM) of the transmission peaks. If the finesse and the free spectral range are known it can be calculated by

$$\delta\nu = \frac{FSR}{\mathcal{F}} = \frac{1}{2\pi\tau}. \quad (5.6)$$

With the measured value for the decay time τ this yields a linewidth

$$\delta\nu = (7.7 \pm 0.1) \text{kHz}. \quad (5.7)$$

Instead of performing a cavity ring-down measurement, it would also be possible to directly measure the cavity linewidth, but in that case the calibration of the axis is not as precise due to the nonlinearity of piezo scans and drifts of the laser during the scan, whereas from the cavity ring-down measurement it can directly be calculated.

⁴ Layertec, Laser Mirror 2×107300 , batch R1008027

5.2.2 Temperature dependence

In order to obtain a good frequency stability of the laser, it is locked to the external high finesse cavity (see Sec 5.3). The achieved frequency stability depends on the stability of the cavity length, which can change due to thermal fluctuations. For this reason it is necessary to temperature stabilize the cavity as explained in Sec. 5.1. In addition to that the knowledge of the temperature dependence of the ULE cavity material can be used to reduce the influence of temperature fluctuations. Such a temperature dependence measurement of the cavity length has been performed and is shown in Fig. 5.4.

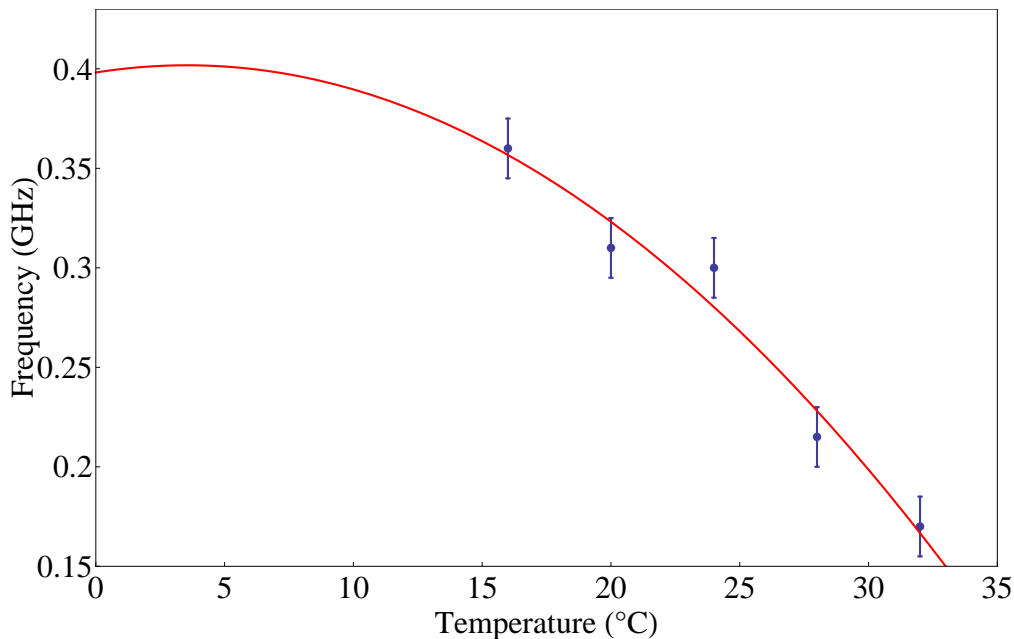


Figure 5.4: Measurement of the frequency drift of the cavity as a function of the temperature.

The measurement was performed by changing the temperature of the cavity in steps of 4° by tuning the setpoint of the temperature stabilization software on the computer. After each change a waiting time of ca. two days was needed, so that the temperature controller could heat/cool to the setpoint and settle there. When the temperature was stable at the desired value, the 1.7 μm laser was locked to the cavity, maintaining the same locking parameters as before to ensure that we always lock to the same TEM00 mode. Then the frequency was measured on the wavemeter. The big error bars are mainly caused by the fluctuations of the wavemeter. In order to estimate the temperature where the thermal expansion coefficient is minimal, the data points were fitted by a parabolic function. On the slope of the function small changes in temperature cause big changes in the cavity length, therefore the least sensitive point to temperature changes is given by the maximum of the curve. It lies at a temperature of 3.5°C . This is the optimum operation temperature for the cavity and the frequency of the laser is most stable. But with the temperature controller this temperature can not be reached and when we are operating so far from room temperature we are very sensitive to its changes. A more precise measurement could be done by using the ion

as a reference. In our actual setup this was not possible because with the implemented single pass AOM configuration we could not shift the frequency back on resonance over a range of 200 MHz. An improvement for the experimental setup, that will soon be realized is the change to a double pass AOM configuration with different central frequency, which gives us a broader range for tuning the frequency.

5.3 Pound-Drever-Hall frequency stabilization

The 4-way cavity is used as external reference to stabilize the frequency of 3 laser systems at 1.7 μm , 1.2 μm and 650 nm by the Pound-Drever-Hall (PDH) technique. After introducing to the general principles of the technique, we describe in more details the 1.7 μm laser locking.

5.3.1 The Pound-Drever-Hall technique

The PDH technique for stabilizing the frequency of a laser was invented by R. Drever and J. Hall, based on a microwave technique previously developed by R.V. Pound. It is based on the principle that the laser frequency is measured by sending it into a cavity, detecting the reflected signal and feeding this measurement back to the laser in order to suppress frequency fluctuations. The error signal for the feedback is generated by phase modulating the laser beam, which leads to sidebands in the reflected signal. By detecting the beatsignal on the carrier and sidebands the relative phase between them is obtained, which gives a direct measure of the detuning from resonance. For a more detailed discussion see Ref. [35, 45, 46].

Theoretical description

If we consider a monochromatic light beam

$$E_{inc} = E_0 e^{i\omega t} \quad (5.8)$$

sent to a cavity, then the total reflected field is given by [41]

$$E_{ref} = E_{inc} r \frac{e^{i\Phi} - 1}{1 - r^2 e^{i\Phi}}. \quad (5.9)$$

The reflected light intensity is symmetric about resonance and can therefore not directly be used for feedback control, because we do not know in which direction the fluctuations occurred. If a phase modulated signal is sent to a cavity, the reflected signal is amplitude modulated, with a modulation proportional to its detuning with respect to the cavity resonance. A more detailed discussion can be found in the Appendix D.

The phase modulated incoming signal, consisting of the carrier at frequency ω and two sidebands at $\omega \pm \Omega$ is then given by

$$E_{inc} = E_0 e^{i(\omega t + \beta \sin(\Omega t))} \quad (5.10)$$

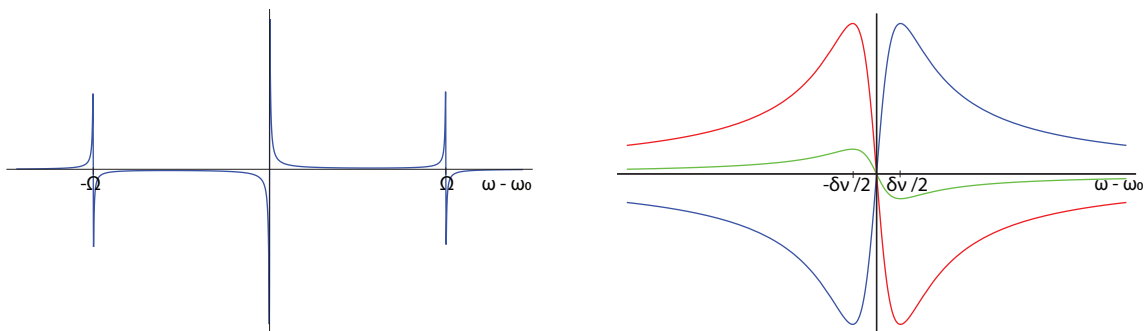
with modulation frequency Ω and modulation index β . The reflected light intensity then contains the beat note oscillating at the modulation frequency Ω , giving a measure for the laser frequency, and terms oscillating at higher orders ($\propto 2\Omega$). In order to isolate the terms oscillating at Ω , we phase match and mix the reflected light intensity with the modulation signal, which leads to

$$\sin(\Omega t) \sin(\Omega' t) = \frac{1}{2} [\cos((\Omega - \Omega')t) - \cos((\Omega + \Omega')t)] \quad (5.11)$$

and send the resulting signal through a low pass filter. For ideal phase matching $\Omega = \Omega'$ and the terms containing the difference $(\Omega - \Omega')$ frequencies will be at DC and pass through the filter, while the sum terms $(\Omega + \Omega')$ will oscillate at high frequencies ($\propto 2\Omega$) and be filtered. The resulting error signal is then given by [45]

$$\epsilon = -2\sqrt{P_C P_S} \text{Im}[F(\omega)F^*(\omega + \Omega) - F^*(\omega)F(\omega - \Omega)], \quad (5.12)$$

in terms of the frequency dependent reflection coefficients $F(\omega) = \frac{E_{ref}}{E_{inc}}$. $P_C = J_0^2(\beta)P_0$ and $P_S = J_1^2(\beta)P_0$ denote the incoming power contained in the carrier and first order sidebands expanded in Bessel functions. Fig. 5.5(a) shows a plot of the error signal given by Eq. (5.12) for a cavity with FSR and \mathcal{F} specified in SubSec. 5.2.1.



(a) Plot of the calculated error signal with the cavity parameters given in SubSec. 5.2.1 and a π -phase shift.

(b) Plot of the calculated error signal close to resonance with local oscillator phases of 0 (red line), $\pi/2$ (green line) and π (blue line).

Figure 5.5: Calculated error signal for a cavity with FSR and \mathcal{F} as specified in SubSec. 5.2.1 for different local oscillator phases.

If the carrier is near resonance,

$$\frac{\omega}{FSR} = 2\pi N + \frac{\delta\omega}{FSR} \quad (5.13)$$

where N is an integer and $\delta\omega$ is the deviation of the laser frequency from resonance, we can assume that the sidebands are completely reflected $F(\omega \pm \Omega) \approx -1$. In this case

$$F(\omega)F^*(\omega + \Omega) - F^*(\omega)F(\omega - \Omega) \approx -i2\text{Im}[F(\omega)] \quad (5.14)$$

is purely imaginary, which reduces the error signal to [45]

$$\epsilon = -4\sqrt{P_C P_S} \text{Im}[F(\omega)]. \quad (5.15)$$

For a high finesse cavity Eq. (5.2) can be approximated by $\mathcal{F} \approx \pi/(1 - r^2)$ and the reflection coefficient reduces to

$$F \approx \frac{i \delta\omega}{\pi \delta\nu} \quad (5.16)$$

where $\delta\nu$ is the cavity linewidth. As long as $\delta\omega \ll \delta\nu$ this approximation holds and with $\omega = 2\pi f$ it yields the following error signal [45]

$$\epsilon = -8\frac{\sqrt{P_C P_S}}{\delta\nu} \delta f. \quad (5.17)$$

This shows that close to resonance the error signal is linearly dependent on the deviation of resonance, which makes it possible to use it for standard feedback control to suppress frequency fluctuations. Its slope depends on the intensity of carrier and sidebands, the laser wavelength and is steeper the higher the finesse is. The sign of the slope depends on the feedback loop that is used and can be chosen by shifting the phase by π . The slope gives a measure for the sensitivity to variations in the laser frequency, thus for a good control it is useful to maximize the slope of the error signal. Usually the wavelength and finesse are fixed, but the slope can be increased by adjusting the sideband power through changing the modulation depth. The optimum can be calculated to be when the power in each sideband is about half the power in the carrier [45]. Another crucial point in order to get a good feedback control is to optimize the phase match between the reflected and the modulating signal.

5.3.2 Experimental realization and results

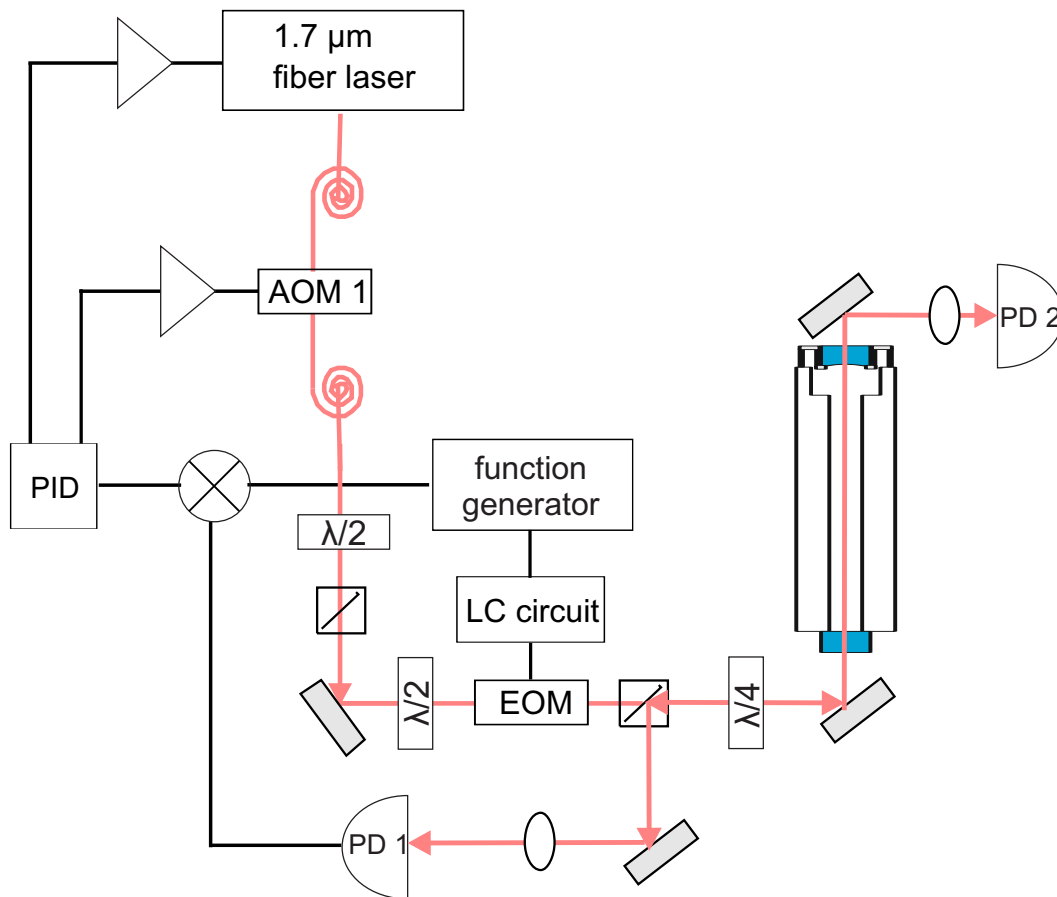


Figure 5.6: Laser setup for the Pound-Drever-Hall locking of the 1.7 μm laser to the cavity. The laser light is modulated at a frequency $\Omega \approx 5$ MHz by an EOM and aligned to the high finesse cavity by optimizing the transmission signal on PD2. The reflected light intensity is detected on the photodiode PD1 and mixed with the modulation signal to generate the error signal which is split into a fast and a slow part and amplified by a PID controller. The fast part is fed back to AOM 1 while the slow part is fed back to the laser piezo.

In order to implement frequency stabilization an AOM (AOM 1) is inserted in the beam path of the $1.7 \mu\text{m}$ laser. While the zeroth order is used for measuring the wavelength, a small fraction of the minus first order is split off by a polarizing beam splitter and sent via a polarization maintaining fiber to the vibration isolation platform where the cavity is located. There, the beam is phase modulated at a frequency of $\Omega \approx 5 \text{ MHz}$ by sending it through an EOM and aligned to the cavity so that the transmission signal is optimized. The setup of the Pound-Drever-Hall locking scheme is shown in Fig. 5.6. For generating the error signal, the intensity of the reflected laser beam is detected on a photodiode with the help of a quarter waveplate and a polarizing beam splitter. The beat signal between reflected carrier and sidebands detected by the PD is then mixed with the modulation signal of the LC-circuit driving the EOM. Phase matching between the two signals is obtained by changing the frequency of the function generator. The demodulated signal is then low-pass filtered at 1.9 MHz in order to isolate the DC signal. A measurement of the generated error signal is shown in Fig. 5.7. It closely resembles the expected signal shown in Fig. 5.5(a), for a π phase-shift. The amplitude of the signal depends on the laser power used for locking to the cavity, the measurement was taken at standard conditions, with a laser power of 1.4 mW before the cavity.

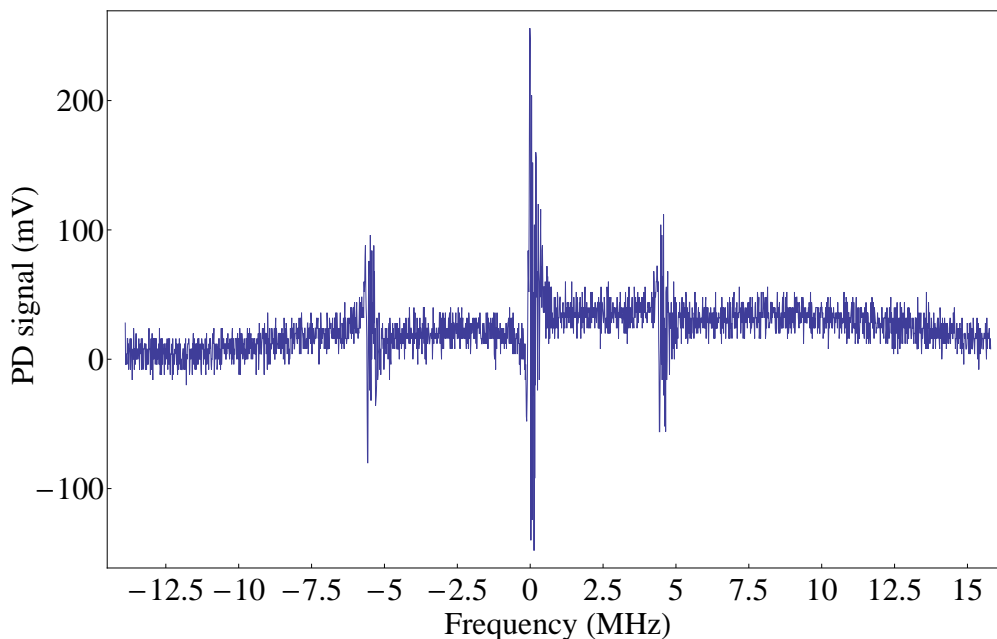


Figure 5.7: Measurement of the generated PDH error signal

Every component in the feedback loop can compensate for fluctuations up to a certain range, its so called bandwidth. The piezo of the laser cavity can only compensate for fluctuations at low frequencies, up to the 1^{st} mechanical resonance, on the order of a few kHz. Therefore, in order to increase the bandwidth of our frequency compensation, we not only perform feedback on the piezo, but also on the AOM (AOM1) which has a larger bandwidth than the piezo. For this reason the error signal is then sent to a PI controller which splits it into low and high frequency regions. The low frequency signal is fed back to a high voltage source driving the piezo of the laser cavity, while the high frequency signal is fed back to the frequency input of the POS box supplying

the RF amplifier driving AOM1. With this two fold feedback we can compensate for frequency fluctuations on a bandwidth up to ca. 100 kHz, where most of the frequency fluctuations occur. In order to further characterize our feedback, we performed a measurement of the noise of the error signal, it is shown in Fig. 5.8.

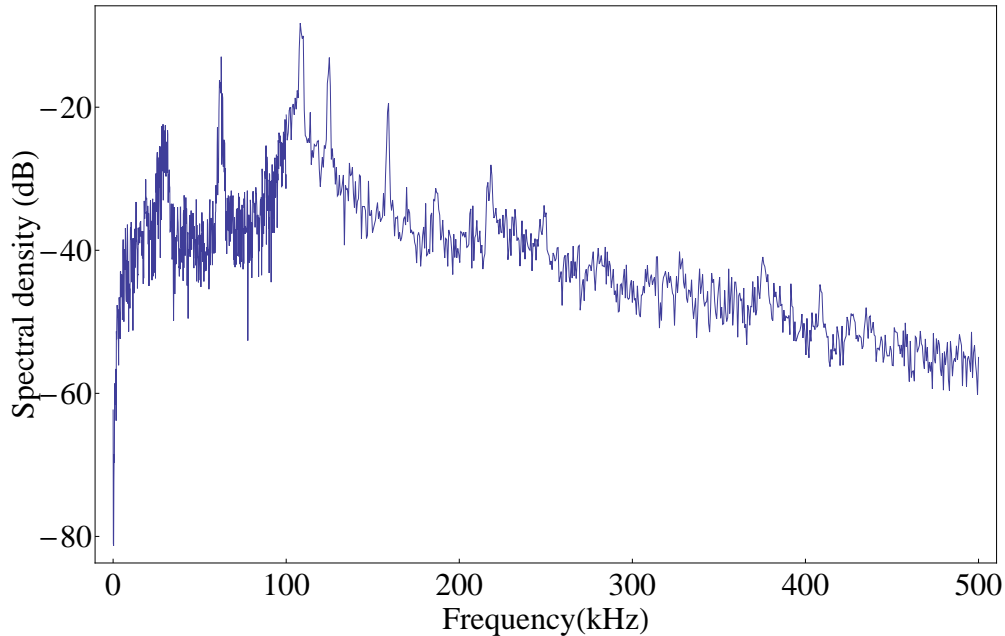


Figure 5.8: Power spectral density of the in-loop error signal

The quoted laser linewidth is specified to be around 20 kHz, therefore the bandwidth of 100kHz should be enough for frequency stabilization. In the measured spectrum of the error signal one can clearly see peaks at 30, 60 and 100 kHz. Further measurements have shown that these peaks result from the fast feedback. When the gain is reduced also the peaks reduce, while with increasing gain the noise is redistributed and the peaks appear. A measurement of the laser intensity at higher frequencies than in Fig. 4.12 shows that this peaks also appear in the intensity when the laser is locked. Which means that obviously the frequency noise introduced by the laser lock converts to intensity noise, after going to the AOM on which we are feeding back the fast part. Nevertheless the observed peaks are about 30 dB below the DC signal and therefore do not significantly contribute to the laser instability. The laser lock is stable over long periods and the laser linewidth can clearly be brought down to the kilohertz regime. For further improving the frequency and intensity stability of the laser system, a more detailed investigation on the noise sources that can be observed as peaks in the intensity (Fig. 4.12) and frequency spectrum (Fig. 5.8) would be necessary. Also additional fiber noise cancelation should enhance intensity stability and further reduce the laser linewidth.

Chapter 6

Spectroscopy and sideband cooling on a single $^{138}\text{Ba}^+$

The main motivation of the work presented in this thesis was to set up a laser system for driving the Barium quadrupole transition and to investigate its properties. After having presented the laser system in the previous sections, we here describe the results of the quadrupole transition spectroscopy.

We demonstrate the observation of quantum jumps on the $|S_{1/2}\rangle$ to $|D_{5/2}\rangle$ transition by tuning the $1.7\ \mu\text{m}$ laser to the quadrupole transition. A scan of the spectrum of the quadrupole transition and Rabi oscillations are also measured. After finding the motional sidebands of the ion in the trap, we then demonstrate sideband cooling up to an observation of 65 % probability in the motional ground state.

6.1 Quantum jumps using the fiber laser

As already discussed in section 4.2.2 the $1.7\ \mu\text{m}$ laser is guided to the trap via a single-mode polarization maintaining fiber after being intensity and frequency stabilized. There, an objective mounted on a translation stage is used to focus the beam at the position of the ion. First the objective was roughly positioned with the help of the 650 nm light, by sending it through the objective and aligning the beam to the trap center. Then, the $1.7\ \mu\text{m}$ beam was sent through and aligned onto the ion by fine positioning of the objective and observing the count rate of the scattered photons on the $|S_{1/2}\rangle$ to $|P_{1/2}\rangle$ transition on the PMT. After having absorbed a $1.7\ \mu\text{m}$ photon the ion is in the $|D_{5/2}\rangle$ state, no more photons are scattered and the count rate on the PMT goes down. As a consequence of the excitation on the quadrupole transition the ion can decay back after some time either due to stimulated emission or to spontaneous decay. With a weak excitation, stimulated emission is negligible, and the count rate shows random dark and bright periods due to quantum jumps. A measurement of quantum jumps is shown in Fig. 6.1.

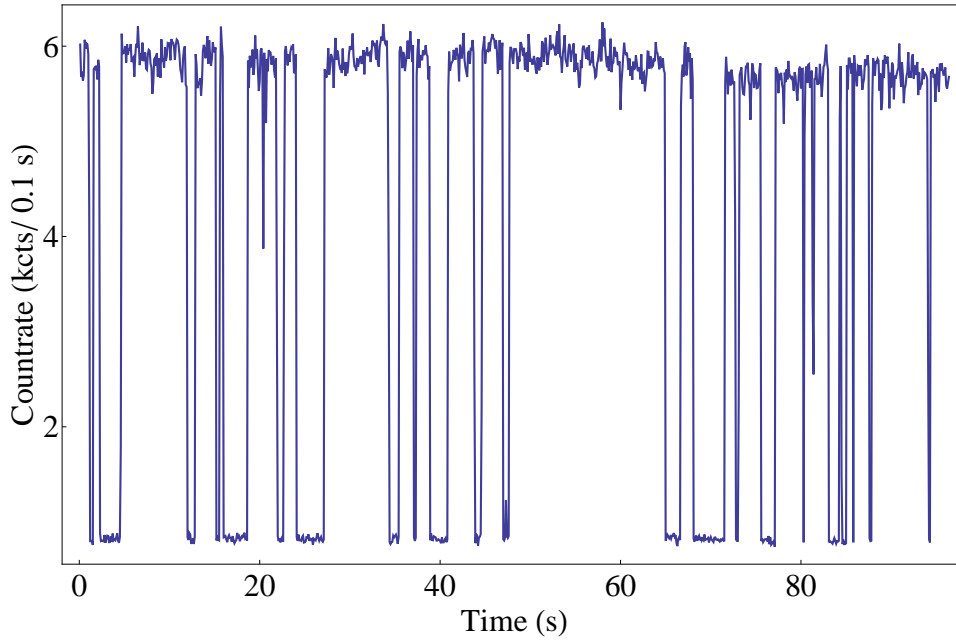


Figure 6.1: Quantum jumps on the $|S_{1/2}\rangle \longleftrightarrow |D_{5/2}\rangle$ transition: The $1.7 \mu\text{m}$ laser is continuously and weakly exciting the quadrupole transition. Photon scattering on the $|S_{1/2}\rangle$ to $|P_{1/2}\rangle$ transition is used for state read out. If the ion is in the $|D_{5/2}\rangle$ state no photons are scattered, while in the $|S_{1/2}\rangle$ state a certain number of counts is detected per 100 ms.

The better the alignment of the laser to the ion, the higher is the excitation probability so that quantum jumps take place more often. When these cycles of excitation and decay occur on timescales lower than the detection time, then the detected count rate will be always at $1/2$ of the maximum, because on average the ion will be half of the time in the upper and half of the time in the lower state. The alignment can be optimized by trying to reach this regime.

6.2 Spectroscopy on the $|S_{1/2}\rangle$ to $|D_{5/2}\rangle$ transition

After optimizing the excitation on the $|S_{1/2}\rangle$ to $|D_{5/2}\rangle$ transition it is then possible to scan the spectrum of the ion on the quadrupole transition. This will enable us to know the position of the carrier and sideband transitions for Rabi and Ramsey experiments and sideband cooling. This procedure is performed before each experiment since the cavity slightly drifts on the order of 3 Hz/s.

In order to scan the spectrum of a specific set of Zeeman sub-levels, the ion first needs to be prepared in a well defined state, then it is excited on the quadrupole transition under investigation and in the last step the resulting state is read out. These steps are realized by applying laser pulse sequences as shown in Fig. 6.2 which are repeated many times.

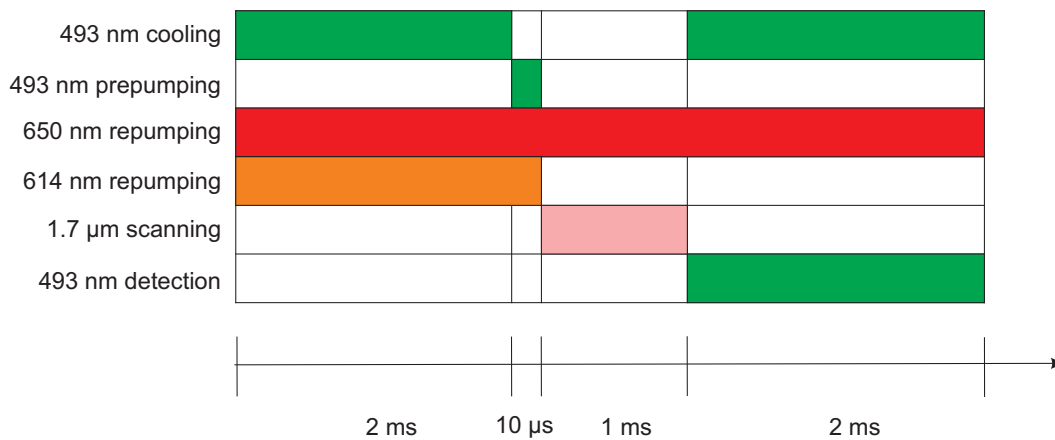


Figure 6.2: Laser pulse sequence used for measuring the spectrum of the quadrupole transition.

First the ion is prepared in the $|S_{1/2}\rangle$ state and Doppler cooled within the Lamb-Dicke regime. Therefore the lasers at 650 nm and 614 nm repump the ion from the $|D_{3/2}\rangle$ and $|D_{5/2}\rangle$ states respectively, back to the electronic ground state $|S_{1/2}\rangle$. Prepumping along the magnetic field prepares it either in the $|S_{1/2}, m = -1/2\rangle$ or in the $|S_{1/2}, m = +1/2\rangle$ state depending if the polarization of the 493 nm light is chosen to be σ^- or σ^+ respectively. After state preparation a 1.7 μm laser pulse is applied to the ion at a certain frequency. Finally the resulting state is detected via the electron shelving method, where the fluorescence light on the dipole transition is measured in order to distinguish whether the ion is still in the ground or in the excited state (see SubSec. 3.1.2). As shown in Fig. 6.2 one measurement has a duration of ca. 5 ms. For each 1.7 μm frequency it is repeated a 100 times and the average excitation probability of the 100 measurements corresponds to one data point. Afterwards the frequency of the quadrupole laser is shifted to the next value and the measurement is repeated. In this way, it is possible to measure the entire spectrum of the quadrupole transition.

As already discussed in section 1.1.2 the presence of an external magnetic field leads to a splitting of the degenerate fine structure states into $(2j + 1)$ sub-states due to the Zeeman effect, as shown in Fig. 6.3. By scanning the 1.7 μm frequency over a range bigger than the Zeeman splitting one will be able to identify the individual transitions from the different Zeeman sub-levels.

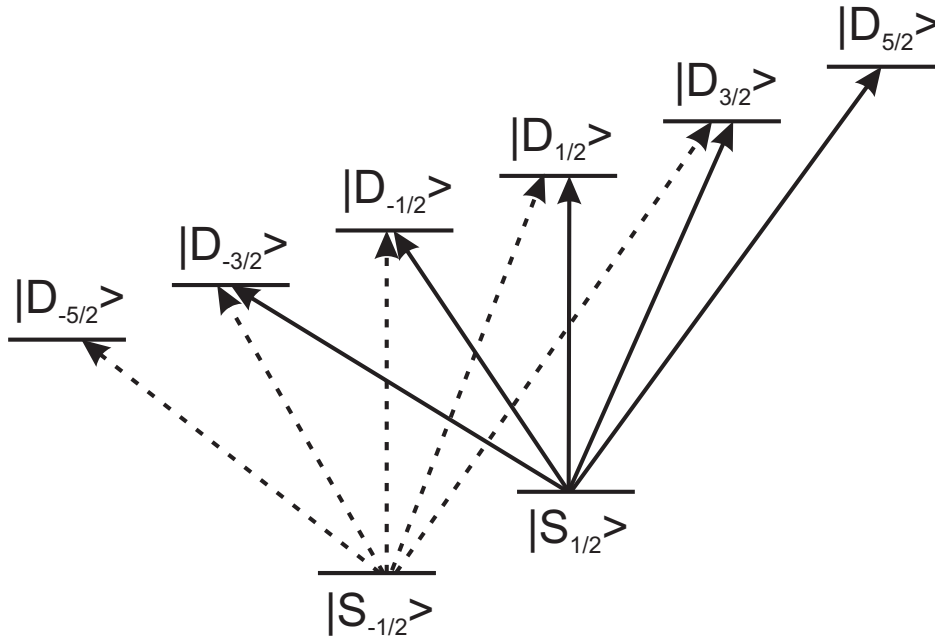


Figure 6.3: Allowed transitions between the Zeeman sub-levels of the $|S_{1/2}\rangle$ state and $|D_{5/2}\rangle$ state. Depending on the prepumping one can excite transitions from $|S_{1/2}, m = +1/2\rangle$ (continuous lines) or from $|S_{1/2}, m = -1/2\rangle$ (dashed lines).

As explained in the Appendix A the coupling strength between the Zeeman sub-levels is proportional to their Clebsch Gordon coefficients and depends on the laser polarization and direction with respect to the magnetic field. If for example the beam axis, the polarization and the magnetic field are mutually orthogonal, only transitions with $\Delta m = \pm 2$ are excited. In order to scan the entire spectrum we used a polarization that allows efficient driving of all the carriers and a 90° angle between magnetic field and beam axis. The spectrum not only reveals these carrier transitions between the Zeeman sub-levels but it also shows the motional sidebands at the axial and radial trap frequencies. The result of a scan is shown in Fig. 6.4.

In order to measure the entire spectrum one needs to scan over a frequency range of about 60 MHz. In our setup we are operating the scanning AOM in single pass configuration and it is not possible to scan around one set central frequency for more than ± 20 MHz without significant power changes, caused by the dependence of the diffraction efficiency on the applied frequency and due to the changed fiber coupling efficiency for the shifted laser beam. Therefore the measurement was divided in three scans with different optimized central frequencies, that were partially overlapped and then combined. A double pass setup will be necessary for sequences combining sideband cooling and state manipulation on the magnetic field insensitive transitions.

This measurement was taken before the DDS board was implemented in the setup, so the AOM frequency was scanned with a resolution of 20 kHz using a function generator and a voltage controlled oscillator. The scan was performed at full laser power, saturating the carrier transitions.

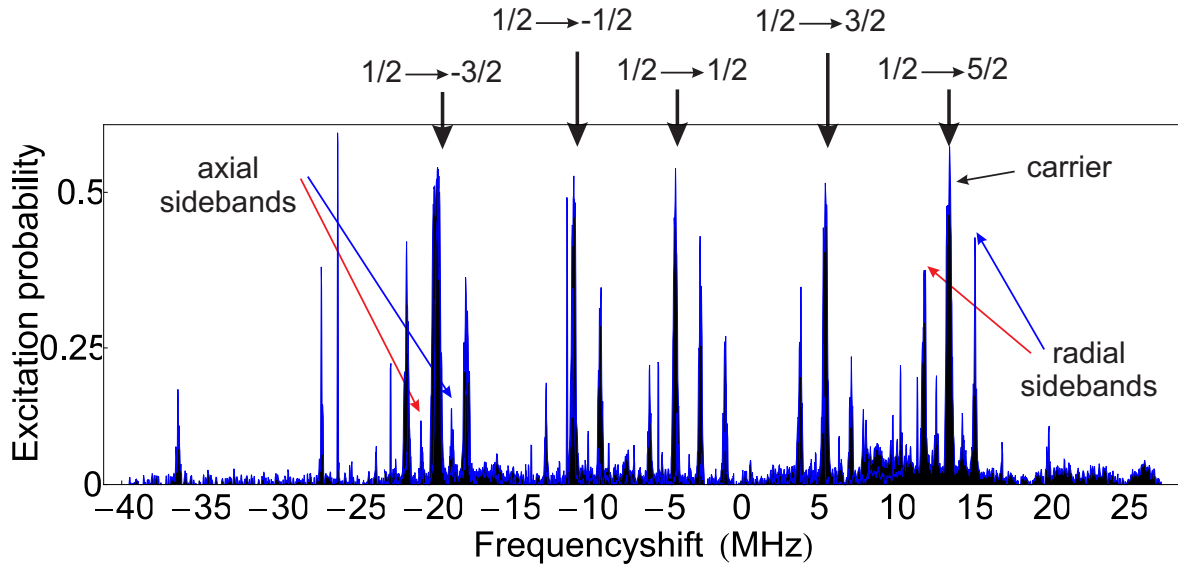


Figure 6.4: Full spectrum of the $|S_{1/2}\rangle \leftrightarrow |D_{5/2}\rangle$ transition with prepumping to the $|S_{1/2}, m = +1/2\rangle$ state. The five carrier transitions with their corresponding red and blue axial and radial sidebands can be identified.

Fig. 6.4 shows a complete scan of the spectrum on the $|S_{1/2}\rangle$ to $|D_{5/2}\rangle$ transition, starting from the $|S_{1/2}, m = +1/2\rangle$ state. The five carrier transitions are equidistantly spread by about (8.3 ± 0.9) MHz which leads to a magnetic field of (4.9 ± 0.6) Gauss according to Eq. (1.2). On the left and right sides of each carrier there are red and blue axial and radial sidebands positioned at a mean distance of $\omega_{axial} = (0.95 \pm 0.06)$ MHz and $\omega_{radial} = (1.8 \pm 0.1)$ MHz. The values are a little lower than expected from the values calculated in section 4.1. In the case of the radial frequency this could be explained by the fact, that the axial confining potential has been neglected in the calculations of the radial trap frequency, if it is taken into account, it reduces it by some percent. A more detailed discussion about this effect can be found in [23]. In this scan we could not resolve the two radial sidebands due to the low resolution and not optimized Doppler cooling settings. They are overlapping and appear in one radial sideband. When the Doppler cooling settings are optimized it is possible to resolve them.

The precision of this measurement is mostly limited by fluctuations of the VCO frequency and could already be improved by implementing the DDS board in the setup. Spectroscopy can also be used to give an upper bound for the laser linewidth. The carrier line has a Lorentzian shape, whose width corresponds to the maximal combined linewidth of the laser and magnetic field fluctuations. Fig 6.5 shows a high resolution measurement of the combined linewidth.

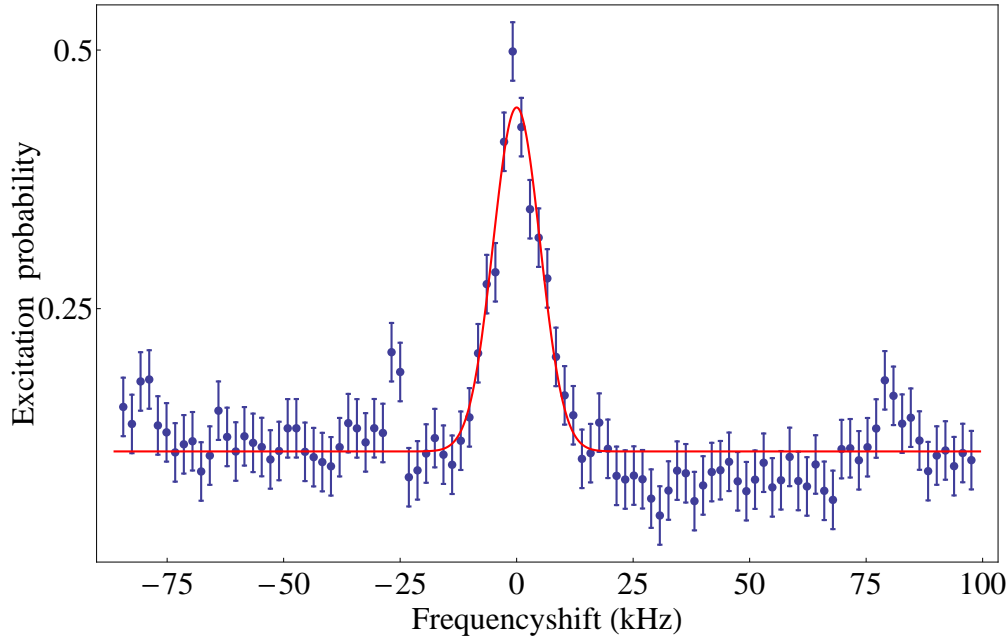


Figure 6.5: Spectral line of the $|S_{1/2}, m = +1/2\rangle$ to $|D_{5/2}, m = +5/2\rangle$ carrier transition measured with a resolution of 1.9 kHz. The FWHM of the Lorentzian fit is 16.6 kHz and gives an upper bound for the combined linewidth of laser and magnetic field.

The linewidth of 16.6 kHz still needs to be improved, it not only limits the resolution of our spectroscopic scans, but it also decreases the coupling strength of the laser to the ion and thus makes sideband cooling less efficient. Furthermore a broad linewidth leads to faster dephasing and shorter coherence times. Further investigations revealed that the linewidth is mostly limited by fluctuations of the magnetic field and could be reduced by improving the stability of the current driving the coils for the magnetic field stabilization.

6.3 Rabi oscillations

After scanning the spectrum and knowing the positions of the carrier transitions it is possible to measure the time evolution of the driven two level atom. For this purpose a similar laser pulse sequence than shown in Fig. 6.2 is used, but here the $1.7 \mu\text{m}$ frequency is set on resonance with one carrier transition. Again this sequence is repeated a 100 times and the average occupation number is taken to obtain one datapoint. Instead of scanning the frequency of the laser, we now set it to the carrier frequency and scan the duration of the pulse. This yields periodical oscillations of the excitation probability as a function of the pulse duration as discussed in SubSec. 3.1.1. The oscillation frequency is given by the Rabi frequency and depends on the Lamb Dicke parameter and the phonon number. A measurement of this so called Rabi oscillations after Doppler cooling is shown in Fig. 6.6.

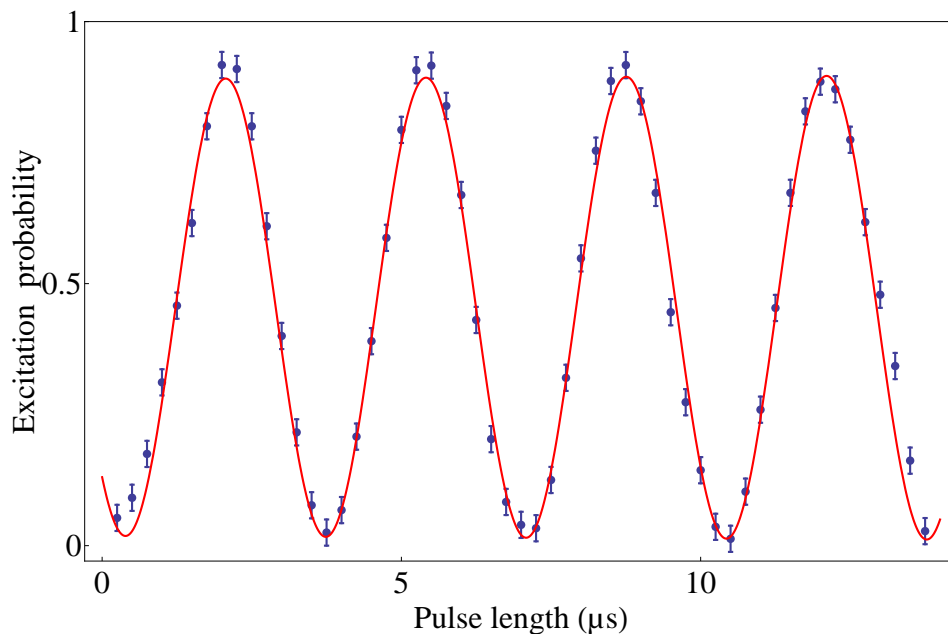


Figure 6.6: Rabi oscillations on the $|S_{1/2}\rangle \longleftrightarrow |D_{5/2}\rangle$ carrier transition for a thermal motional state after Doppler cooling.

From the measured data in Fig. 6.6 one can see that the contrast of the oscillations is not one and thus the population is not completely transferred to the excited state. For longer pulse durations than shown in Fig. 6.6 it can be observed that the oscillations are slowly damping out with time. This damping is related to the dependence of the Rabi frequencies on the motional state and is proportional to the mean phonon number $\langle n \rangle$. The loss of contrast results from the dephasing of the oscillations of populations in different vibrational states [21]. For this reason Rabi oscillations provide a tool to optimize Doppler cooling. By changing the detuning and intensity of the cooling laser, it is possible to minimize the damping rate. However since the Rabi frequency also depends on the laser detuning from resonance and on its intensity, it is sensitive to magnetic field fluctuations that broaden the laser linewidth. This influences the oscillations together with intensity fluctuations and leads to damping. Sideband cooling, magnetic field and intensity stability will help to get a better contrast.

For sufficiently high n the damped Rabi oscillations can be approximated by an exponentially decaying sinusoidal oscillation as shown by the fit to the data. For a more detailed evaluation of the damped Rabi oscillations a more complicated model should be used, describing the superposition of the oscillations of all vibrational states. A detailed discussion for such a model can be found in the Appendix of [21].

6.4 Sideband cooling

As already discussed earlier in Sec. 3.2 due to the Doppler cooling limit it is not possible to cool the ion to the ground state just by this technique alone. The mean phonon number of 5 to 10 after Doppler cooling can be further reduced by additional sideband cooling. Combining these two methods makes it possible to cool the ion to its motional ground state with high probability.

Once the carrier and sideband transitions have been determined by scanning the spectrum, one can apply a laser pulse sequence for cooling either the radial, the axial, or both modes to the ground state, such a pulse sequence is shown in Fig. 6.7.

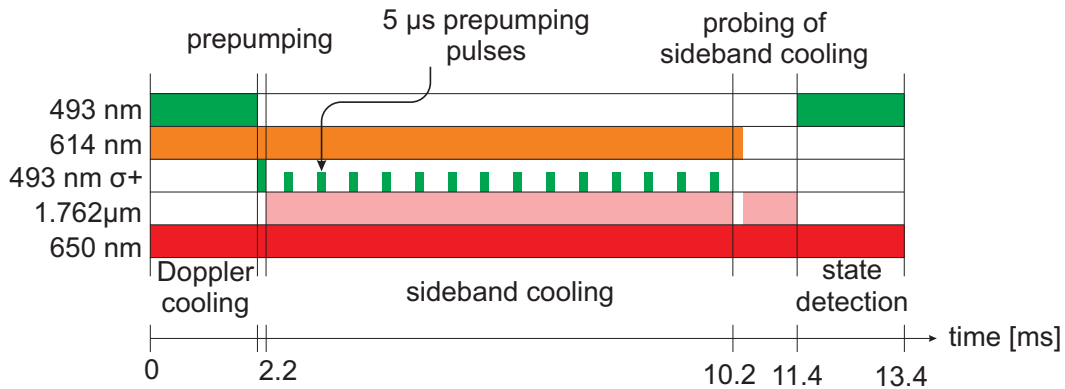


Figure 6.7: Laser pulse sequence for sideband cooling.

The sequence is again very similar to the ones used before, but in this case the 1.7 μm laser frequency is set on resonance with the axial or radial red sideband transition, depending on which mode one wishes to be cooled. In section 3.2.2 it was already shown that one quantum of motion can be reduced by excitation on the red sideband and spontaneous decay on the carrier transition. Due to the long lifetime of the $|D_{5/2}\rangle$ state this process can take several seconds. In order to increase the cooling efficiency repumping with the 614 nm laser is used to shorten the decay back to the electronic ground state. A few short prepumping pulses homogeneously distributed over the cooling time ensure that we always start from the resonant $|S_{1/2}\rangle$ Zeeman sub-level and hence further increase the cooling rate. Without these prepumping pulses the electron could get stuck in the off-resonant $|S_{1/2}\rangle$ Zeeman sub-level, due to spontaneous decay from the $|P_{3/2}\rangle$ into the $|D_{3/2}\rangle$ level and subsequent repumping to the $|P_{1/2}\rangle$ level, from where it can decay into both Zeeman sub-levels of the electronic ground state. After Doppler and sideband cooling the mean phonon number and the ground state probability are measured by probing the excitation probability on the red and blue sidebands and comparing them (see SubSec. 3.2.2).

The best transitions for sideband cooling are the $|S_{1/2}, m = -1/2\rangle$ to $|D_{5/2}, m = -5/2\rangle$ and the $|S_{1/2}, m = +1/2\rangle$ to $|D_{5/2}, m = +5/2\rangle$ transitions, because together with the repumping step to the $|P_{3/2}\rangle$ level they form a closed transition for cooling. For the following measurement the $|S_{1/2}, m = +1/2\rangle$ to $|D_{5/2}, m = +5/2\rangle$ transition was used.

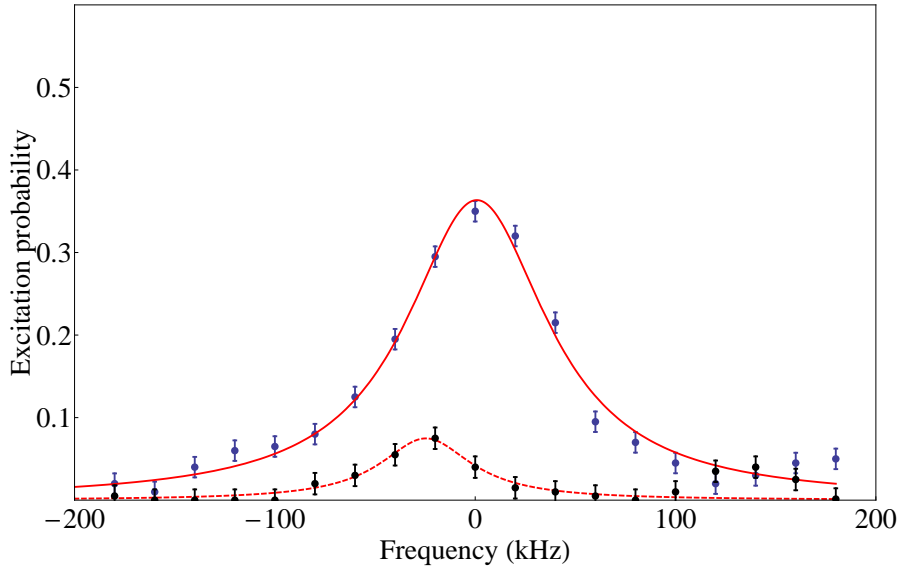


Figure 6.8: Red axial sideband before (blue datapoints) and after sideband cooling (black datapoints) fitted by a Lorentzian distribution.

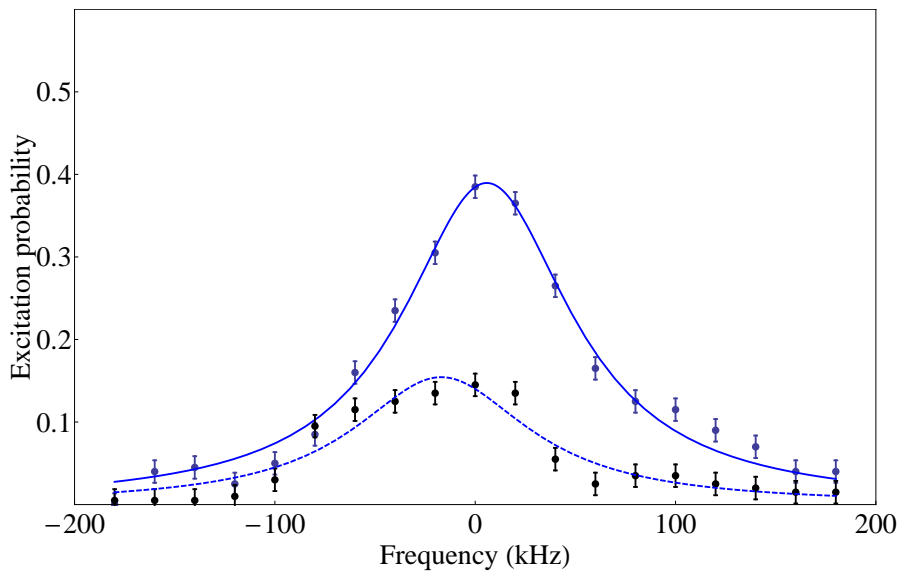


Figure 6.9: Blue axial sideband before (blue datapoints) and after sideband cooling (black datapoints) fitted by a Lorentzian distribution.

Fig. 6.8 and 6.9 show the absorption spectra of the red and blue axial sidebands before and after sideband cooling. The big uncertainties in frequency direction may be caused by shifts of the VCO or the trap frequency. The area under the curves corresponds to the excited state probability. From the ratio of the red and blue sidebands excitation probability the mean phonon number can be calculated according to Eq. (3.21) and Eq. (3.22) from Subsec. 3.2.2. The measured data yield a mean phonon number $\langle n \rangle$ of 0.6 phonons. The phonon number follows a discrete geometric distribution, therefore it is possible to calculate the ground state probability from the measured mean phonon number. The probability density function for a geometric distribution is given by

$$P(n) = p(1 - p)^n \quad (6.1)$$

with the mean value of

$$\langle n \rangle = \frac{1-p}{p}. \quad (6.2)$$

A comparison of Eq. (6.2) with Eq. (3.22) leads to the following relations

$$p = 1 - R \quad P(n) = (1 - R)R^n. \quad (6.3)$$

The ground state probability is given by $P(0) = 1 - R$ which leads to a measured value of ca. 65 %. This was only a first demonstration of sideband cooling, the cooling efficiency still needs to be optimized to achieve a good state preparation. In the Calcium experiments of our research group ground state cooling up to a 99 % probability can be obtained. If we are able to decrease the combined laser linewidth below 1 kHz by reducing the magnetic field fluctuations or line triggering, we should in principle also be able to achieve ground state probabilities of more than 90 %.

Chapter 7

Summary and outlook

Due to technical limitations until now it was very difficult to realize a well controllable laser system to excite the Barium quadrupolar transition at $1.7 \mu\text{m}$ in our setup. Within this thesis we have shown a frequency and intensity stabilized fiber-laser setup for the wavelength of the $|S_{1/2}\rangle \longleftrightarrow |D_{5/2}\rangle$ transition. The availability of the $1.7 \mu\text{m}$ laser opens many new experimental possibilities for our project.

Although cooling below the Doppler limit could be realized, until now ground state cooling of the Barium ions has not been possible in our project. The implementation of the quadrupole-transition laser enables us to perform sideband cooling and a ground state probability of 65 % could be obtained. Cooling close to the motional ground state leads to better localization and thus gives us better control over the system. Furthermore, spectroscopic investigations on the $|S_{1/2}\rangle \longleftrightarrow |D_{5/2}\rangle$ transition have been performed and we could show that state preparation, manipulation and read out are possible.

Nevertheless the laser system can and needs to be improved. First of all the laser linewidth needs to be reduced to allow more precise spectroscopic scans and a stronger excitation of the ion. Another important improvement would be to identify the cause of the 80 MHz amplitude modulation, which can potentially cause unwanted effects. For this reason we either think about internal changes in the laser system or implementing a feed-forward stabilization.

Besides the improvements of the laser system there are some further experimental tools that will soon be implemented. For example, Ramsey spectroscopy is needed to stabilize the phase relation between different laser pulses and to measure our coherence times. Another important feature would be to implement single ion addressing, in order to manipulate a number of ions in one trap individually.

With the new laser system we can think of a series of possible future experiments that require the controlled manipulation of the quadrupole transition. One could use the quadrupole transition for remote entanglement in the two different traps according to the Cabrillo scheme as described in section 1.2. Here the $|D_{5/2}\rangle$ state could either be used as metastable state $|e\rangle$ or the states $|S_{1/2}, m = -1/2\rangle$ and $|S_{1/2}, m = +1/2\rangle$ are used as two ground states $|g\rangle$ and $|e\rangle$ and the $1.7 \mu\text{m}$ laser is needed for state read out by the electron shelving method. In principle, one could also repeat the QED-experiments using the quadrupole transition to measure the mirror induced level shift of the $|S_{1/2}\rangle$ ground state via Ramsey spectroscopy. Furthermore it opens the door for

possible quantum information experiments using this long lived state as a qubit. These are just some of many examples of possible applications.

Bibliography

- [1] E. Schrödinger, “Are there quantum jumps?,” *Br. J. Philosophy Sci.*, vol. 3, pp. 109–123, 1952.
- [2] NIST, “Physical reference data, handbook of basic atomic spectroscopic data.” <http://www.nist.gov/pml/data/handbook/index.cfm>, 2005.
- [3] B. Appasamy, *Ein Farbzentrenringlaser für die Spektroskopie am einzelnen Ba⁺-Ion*. Diplomarbeit, Universität Hamburg, März 1991.
- [4] A. A. Madej and J. D. Sankey, “Quantum jumps and the single trapped barium ion: Determination of collisional quenching rates for the $5d^2D_{5/2}$ level,” *Phys. Rev. A*, vol. 41, pp. 2621–2630, Mar 1990.
- [5] N. Yu, W. Nagourney, and H. Dehmelt, “Radiative Lifetime Measurement of the Ba⁺ Metastable D_{3/2} State,” *Phys. Rev. Lett.*, vol. 78, pp. 4898–4901, Jun 1997.
- [6] A. Gallagher, “Oscillator Strengths of Ca II, Sr II, and Ba II,” *Phys. Rev.*, vol. 157, pp. 24–30, May 1967.
- [7] J. Schulz, *Modulationsspektroskopie an einem einzelnen Ba⁺-Ion*. Diplomarbeit, Universität Hamburg, März 1998.
- [8] H. Haken und H. C. Wolf, *Atom- und Quantenphysik*. Springer-Verlag, 5. Auflage, 1993.
- [9] J. Eschner, C. Raab, F. Schmidt-Kaler, and R. Blatt, “Light interference from single atoms and their mirror images,” *Nature*, vol. 413, pp. 495–498, Oct. 2001.
- [10] M. A. Wilson, P. Bushev, J. Eschner, F. Schmidt-Kaler, C. Becher, R. Blatt, and U. Dorner, “Vacuum-Field Level Shifts in a Single Trapped Ion Mediated by a Single Distant Mirror,” *Phys. Rev. Lett.*, vol. 91, p. 213602, Nov 2003.
- [11] P. Bushev, A. Wilson, J. Eschner, C. Raab, F. Schmidt-Kaler, C. Becher, and R. Blatt, “Forces between a Single Atom and Its Distant Mirror Image,” *Phys. Rev. Lett.*, vol. 92, p. 223602, Jun 2004.
- [12] P. Bushev, D. Rotter, A. Wilson, F. Dubin, C. Becher, J. Eschner, R. Blatt, V. Steixner, P. Rabl, and P. Zoller, “Feedback Cooling of a Single Trapped Ion,” *Phys. Rev. Lett.*, vol. 96, p. 043003, Feb 2006.

-
- [13] C. Cabrillo, J. I. Cirac, P. García-Fernández, and P. Zoller, “Creation of entangled states of distant atoms by interference,” *Phys. Rev. A*, vol. 59, pp. 1025–1033, Feb 1999.
- [14] S. Zippilli, G. A. Olivares-Rentería, G. Morigi, C. Schuck, F. Rohde, and J. Eschner, “Entanglement of distant atoms by projective measurement: the role of detection efficiency,” *New Journal of Physics*, vol. 10, no. 10, p. 103003.
- [15] S. Gerber, D. Rotter, M. Hennrich, R. Blatt, F. Rohde, C. Schuck, M. Almendros, R. Gehr, F. Dubin, and J. Eschner, “Quantum interference from remotely trapped ions,” *New Journal of Physics*, vol. 11, no. 1, p. 013032, 2009.
- [16] F. Dubin, D. Rotter, M. Mukherjee, S. Gerber, and R. Blatt, “Single-Ion Two-Photon Source,” *Phys. Rev. Lett.*, vol. 99, p. 183001, Oct 2007.
- [17] W. Paul, “Electromagnetic traps for charged and neutral particles,” *Rev. Mod. Phys.*, vol. 62, pp. 531–540, Jul 1990.
- [18] C. J. Foot, *Atomic Physics*. Oxford University Press, 2005.
- [19] M. Brownnutt, *⁸⁸Sr⁺ ion trapping techniques and technologies for quantum information processing*. PhD thesis, Imperial College London, 2007.
- [20] G. Morigi, F. Schmidt-Kraler, and R. Blatt, “Laser cooling of trapped ions,” *J. Opt. Soc. Am. B*, vol. 20, no. 5.
- [21] C. F. Roos, *Controlling the quantum state of trapped ions*. PhD thesis, Leopold-Franzens-Universität Innsbruck, 2000.
- [22] D. Leibfried, R. Blatt, C. Monroe, and D. Wineland, “Quantum dynamics of single trapped ions,” *Rev. Mod. Phys.*, vol. 75, pp. 281–324, Mar 2003.
- [23] D. Rotter, *Quantum feedback and quantum correlation measurements with a single Barium ion*. PhD thesis, Leopold-Franzens-Universität Innsbruck, 2008.
- [24] D. Walls and G. J. Milburn, *Quantum Optics*. Springer-Verlag Berlin Heidelberg, 2008.
- [25] H. Häffner, C. F. Roos, and R. Blatt, “Quantum computing with trapped ions,” *Physics Reports-review Section of Physics Letters*, vol. 469, pp. 155–203.
- [26] L. Deslauriers, *Cooling and Heating of the Quantum Motion of Trapped Cd⁺ Ions*. PhD thesis, University of Michigan, 2006.
- [27] H. G. Dehmelt, “Proposed $10^{14} Dv < v$ Laser Fluorescence Spectroscopy on Tl^+ Mono-Ion Oscillator II (spontaneous quantum jumps),” *Bull. Am. Phys. Soc.*, vol. 20, 1975.
- [28] W. Nagourney, J. Sandberg, and H. Dehmelt, “Shelved optical electron amplifier: Observation of quantum jumps,” *Phys. Rev. Lett.*, vol. 56, pp. 2797–2799, Jun 1986.

- [29] W. Neuhauser, M. Hohenstatt, P.E. Toschek and H.G. Dehmelt, "Optical-Sideband Cooling of Visible Atom Cloud Confined in Parabolic Well," *Physical Review Letters*, vol. 41, no. 4, p. 233, 1978.
- [30] D.J. Wineland, R.E. Drullinger and F.L. Walls, "Radiation-Pressure Cooling of Bound Resonant Absorbers," *Physical Review Letters*, vol. 40, no. 25, p. 1639, 1978.
- [31] S. Stenholm, "The semiclassical theory of laser cooling," *Rev. Mod. Phys.*, vol. 58, pp. 699–739, Jul 1986.
- [32] S. Gerber, *Quantum Correlation Experiments with Resonance Fluorescence Photons of single Barium Ions*. PhD thesis, Leopold-Franzens-Universität Innsbruck, 2010.
- [33] J. Bolle, *Spektroskopie und nichtklassische Fluoreszenzeigenschaften von einzelnen gespeicherten Barium-Ionen*. PhD thesis, Leopold Franzens Universität Innsbruck, 1998.
- [34] H. Langfischer, *Frequenzstabilisierung eines Diodenlasers bei 650 nm zur Spektroskopie an einzelnen Barium-Ionen*. Diplomarbeit, Leopold Franzens Universität Innsbruck, April 1998.
- [35] R. W. P. Drever, J. L. Hall and F. V. Kowalski, "Laser phase and frequency stabilization using an optical resonator," *Appl. Phys. B*, vol. 31, no. 97, 1983.
- [36] L. S. Ma, Ph. Courteille, G. Ritter, W. Neuhauser and R. Blatt, "Spectroscopy of Te² with modulation transfer: Reference lines for precision spectroscopy in Yb⁺ at 467 nm," *Appl. Phys. B*, vol. 57, no. 683, 1993.
- [37] P. Schindler, *Frequency synthesis and pulse shaping for quantum information processing with trapped ions*. Diploma thesis, Leopold Franzens Universität Innsbruck, September 2008.
- [38] J. Bechhoefer, "Feedback for physicists: A tutorial essay on control," *Rev. Mod. Phys.*, vol. 77, pp. 783–836, Aug 2005.
- [39] J. Doyle, B. Francis and A. Tannenbaum, *Feedback Control Theory*. Macmillan Publishing Co., 1990.
- [40] W. Schumacher und W. Leonhard, *Grundlagen der Regelungstechnik*. Institut für Regelungstechnik, Technische Universität Braunschweig, 2008.
- [41] G. Kirchmair, *Frequency stabilization of a Titanium-Sapphire laser for precision spectroscopy on Calcium ions*. Diploma thesis, Leopold Franzens University of Innsbruck, Nov 2006.
- [42] J. Ziegler and N. Nichols, "Optimum settings for automatic controllers," *Trans. ASME*, vol. 64, pp. 759–768, 1942.
- [43] J. Benhelm, *Precision spectroscopy and quantum information processing with trapped Calcium ions*. PhD thesis, Leopold Franzens Universität Innsbruck, 2008.

-
- [44] M. Chwalla, *Precision spectroscopy with $^{40}\text{Ca}^+$ ions in a Paul trap*. PhD thesis, Leopold Franzens Universität Innsbruck, 2009.
- [45] E. D. Black, “An introduction to Pound Drever Hall frequency stabilization,” *Am. J. Phys.*, vol. 69, no. 1, 2001.
- [46] E. D. Black, “Notes on the Pound Drever Hall technique,” *Technical Note of the LIGO Project*, 1998.
- [47] D. James, “Quantum dynamics of cold trapped ions with application to quantum computation,” *Applied Physics B: Lasers and Optics*, vol. 66, pp. 181–190, 1998.
- [48] W. R. Johnson, *Atomic Structure Theory - Lectures on Atomic Physics*. Springer Berlin Heidelberg, 2007.
- [49] C. Eckart, “The Application of Group Theory to the Quantum Dynamics of Monatomic Systems,” *Rev. Mod. Phys.*, vol. 2, pp. 305–380, 1930.
- [50] E. Wigner, “Gruppentheorie und ihre Anwendung auf die Quantenmechanik der Atomspektren,” 1931.

Appendix A

The quadrupole transition

In this section we have a closer look at the interaction Hamiltonian for the special case of a quadrupole transition $|S, m\rangle \leftrightarrow |D, m'\rangle$. In this case the induced electric-quadrupolar moment q couples to the gradient of the electromagnetic field. The corresponding Hamiltonian for a single outer shell electron is given by [22]

$$H_q = \sum_{i,j} eq_{i,j} \frac{\partial}{\partial x_i} E_j \quad (\text{A.1})$$

with the quadrupole tensor

$$q_{i,j} = \frac{1}{2} \left(x_i x_j - \frac{1}{3} \delta_{ij} \mathbf{r}^2 \right). \quad (\text{A.2})$$

Comparison with the general interaction Hamiltonian of Eq. (3.4) leads to the following definition of the Rabi frequency [47]

$$\Omega = \left| \frac{eE_0}{2\hbar} \langle S, m | (\boldsymbol{\epsilon} \cdot \mathbf{r}) (\mathbf{k} \cdot \mathbf{r}) | D, m' \rangle \right|$$

where m is the magnetic quantum number. By means of the Wigner-Eckart theorem¹ [49, 50] the above expression can be rewritten as

$$\Omega = \left| \frac{eE_0}{2\hbar} \langle S || r^2 \mathbf{C}^{(2)} || D \rangle \sum_{\mathbf{q}=-2}^2 \begin{pmatrix} 1/2 & 2 & 5/2 \\ -m & q & m' \end{pmatrix} \mathbf{g}^{(\mathbf{q})} \right| \quad (\text{A.4})$$

with the Wigner-3j-symbols in round brackets and the reduced matrix element $\langle S || r^2 \mathbf{C}^{(2)} || D \rangle$.

The geometry dependent factor is defined by $g^{(q)} = c_{i,j}^{(q)} \epsilon_i n_j$. Explicit calculations of the second rank tensor $c_{i,j}^{(q)}$ can be found in [47].

The reduced matrix element is related to the Einstein A coefficient of the transition via the relation [47]

¹ The Wigner-Eckart theorem is [48]

$$\langle j, m | Q_{l,q} | j', m' \rangle = (-1)^{j-m} \langle j || Q_l || j' \rangle \begin{pmatrix} j & l & j' \\ -m & q & m' \end{pmatrix} \quad (\text{A.3})$$

$$A = \frac{c\alpha k^5}{15(2j'+1)} \left| \langle S || r^2 \mathbf{C}^{(2)} || D \rangle \right|^2 \quad (\text{A.5})$$

with the fine structure constant α . Inserting Eq. (A.5) into the expression for the Rabi frequency (A.4) yields [21]

$$\Omega = \frac{eE}{\hbar} \sqrt{\frac{5\lambda^3 A}{64\pi^3 c\alpha}} \quad (\text{A.6})$$

for the $|S_{1/2}, m = -1/2\rangle \longleftrightarrow |D_{5/2}, m = -5/2\rangle$ transition in the case of optimal coupling.

Appendix B

Doppler cooling limit

As already discussed in SubSec. 3.2.1, the average radiation pressure force acting on the ion is given by [22]

$$\left(\frac{dp}{dt}\right)_a \sim F_a = \hbar k \Gamma \rho_{ee} \quad (\text{B.1})$$

with the excited state probability ρ_{ee} , saturation parameter s and Doppler shift δ_{eff}

$$\rho_{ee} = \frac{s/2}{1 + s + (2\delta_{eff}/\Gamma)^2} \quad s = \frac{2|\Omega|^2}{\Gamma^2} \quad \delta_{eff} = \Delta - kv. \quad (\text{B.2})$$

In the case of a weakly driven cooling transition, or low saturation respectively, ρ_{ee} simplifies to [21]

$$\rho_{ee} = \frac{\Omega^2}{\Gamma^2 + 4(\Delta - kv)^2}.$$

Close to the final temperature reached by laser cooling, when the velocity is already small, the radiation pressure force F_a can be linearized around $v = 0$

$$F_a = F_0 + \left.\frac{dF_a}{dv}\right|_{v=0} v \quad \text{with} \quad F_0 = \hbar k \Gamma \frac{\Omega^2}{\Gamma^2 + 4\Delta^2} \quad \text{and} \quad \left.\frac{dF_a}{dv}\right|_{v=0} = F_0 \frac{8k\Delta}{\Gamma^2 + 4\Delta^2}$$

where F_0 denotes the time-averaged radiation pressure that displaces the ion slightly from the trap center. If the laser detuning Δ is negative, then the cooling force will provide a viscous drag [21]. The cooling rate, averaged over many oscillation periods, is then

$$\dot{E}_c = \langle F_a v \rangle = \left\langle \left(F_0 + \left.\frac{dF_a}{dv}\right|_{v=0} v \right) v \right\rangle = \left.\frac{dF_a}{dv}\right|_{v=0} \langle v^2 \rangle \quad (\text{B.3})$$

since $\langle v \rangle = 0$ for a trapped particle. In principle the ion could be cooled to zero energy, if the random nature of the light-scattering events is not considered. But in reality this can never be the case because absorption and emission processes will continue even if it has zero velocity. Since the spontaneously emitted photons are isotropically distributed, the average change of momentum is zero, but the momentum undergoes

diffusion $\langle \Delta p^2 \rangle \neq 0$, what can lead to heating with a probability proportional to η^2 if the phonon number n changes. Also the absorption of photons leads to momentum kicks, but only along the direction of the cooling beam, this again gives rise to diffusion [22]. The heating rate for low velocities takes the form

$$\dot{E}_h = \frac{1}{2m} \frac{d}{dt} \langle p^2 \rangle = \dot{E}_{abs} + \dot{E}_{em} \simeq \frac{(\hbar k)^2}{2m} \Gamma \rho_{ee}(v=0) \quad (\text{B.4})$$

If heating and cooling rate equal each other, equilibrium will be reached [21]

$$\left. \frac{dF_a}{dv} \right|_{v=0} \langle v^2 \rangle = \frac{(\hbar k)^2}{2m} \Gamma \rho_{ee}(v=0) \quad (\text{B.5})$$

and the cooling limit can be estimated by using the relation $m \langle v^2 \rangle = k_B T$

$$k_B T = \frac{\hbar \Gamma}{4} \left(\frac{\Gamma}{-2\Delta} + \frac{-2\Delta}{\Gamma} \right) \quad (\text{B.6})$$

where k_B is the Boltzmann constant. The lowest temperature will be

$$T_{min} = \frac{\hbar \Gamma}{2k_B} \quad (\text{B.7})$$

for a laser detuning $\Delta = \frac{-\Gamma}{2}$ [21].

The fact that absorption and emission momentum kicks occur at the same rate but in different directions, can be taken into account by scaling the emission term with the geometry factor ξ , who gives the component of the emission along the beam direction. Then the minimum temperature is given by [22]

$$T_{min} = \frac{\hbar \Gamma}{4k_B} (1 + \xi) \quad (\text{B.8})$$

where for dipole radiation $\xi = 2/5$.

Appendix C

Feedback control theory

In control theory it is very convenient to analyze systems in the frequency domain, therefore Laplace transforms¹ are used to describe the single parts of the feedback loop. $Y(s)$ for example denotes the Laplace transform of the real output signal $y(t)$. In the transform space the complex transfer function $G(s)$ is then given by the ratio of output to input

$$G(s) = \frac{Y(s)}{U(s)},$$

it determines the capability of the system to follow the input signal. The implicit frequency dependence can be made explicit by evaluating it at $s=i\omega$. The transfer function of elements in series is given by the product of their transfer functions. Thus without considering the disturbances $D(s)$ in the first place, the transfer function of the control loop shown in Fig. 4.10 is given by [38]

$$T(s)_{open} = \frac{Y(s)}{E(s)} = K(s)G(s) \quad (C.1)$$

for the open loop and by

$$T(s)_{closed} = \frac{Y(s)}{R(s)} = \frac{K(s)G(s)}{1 + K(s)G(s)} \quad (C.2)$$

for the closed loop respectively. Expression C.2 follows from C.1 by inserting the relation $E(s)=R(s)-Y(s)$. Due to the subtraction of the two signals feedback of this kind is called “negative feedback”, it gives a positive signal when the output is lower than the reference and vice versa. Therefore the output signal is always pushed towards the setpoint and the controlled system follows changes of the input faster than the uncontrolled one. In the case of laser power stabilization, though, this is not really required, because the reference signal in general stays the same[38]. In this case it is important to compensate as fast as possible for perturbations acting on the system. So if now also the disturbances $D(s)$ are taken into account the complete control system shown in Fig. 4.10 is described by [40]

¹ The Laplace transform of a signal $y(t)$ is given by $\mathcal{L}[y(t)] = Y(s) = \int_0^\infty y(t)e^{-st}dt$.

$$Y(s) = \frac{K(s)G(s)}{1 + K(s)G(s)}R(s) + \frac{G(s)}{1 + K(s)G(s)}D(s) = T(s)_{closed}R(s) + S(s)G(s)D(s) \quad (\text{C.3})$$

where $S(s)$ is a measure for the systems sensibility to perturbations and is defined by

$$S(s) = \frac{1}{G(s)} \frac{Y(s)}{D(s)} \Big|_{R(s)=0}$$

Appendix D

Pound-Drever-Hall error signal

If we consider a incoming monochromatic light beam

$$E_{inc} = E_0 e^{i\omega t}, \quad (\text{D.1})$$

it can only pass through the cavity if twice the cavity length corresponds to a multiple integer of the lights wavelength $2L = n\lambda$ or if the laser frequency is a integer number times the cavities free spectral range $\omega = nFSR$ respectively. For a symmetric loss less cavity with reflection and transmission coefficients

$$r_1 = r_2 = r \quad t_1 = t_2 = t \quad r^2 + t^2 = 1, \quad (\text{D.2})$$

all the light is transmitted in this resonant case. Out of resonance though the reflected light intensity is symmetrically increasing around resonance. The electric field of the reflected signal consists of a promptly reflected part, bouncing off the first mirror, and a part leaking out of the cavity after each roundtrip. The promptly reflected beam has a phase shift of π compared to the incoming beam, whereas the light traveling through the cavity accumulates a phase [46]

$$\Phi = \omega T_\Phi = 2\pi \frac{2L}{\lambda} = \frac{\omega}{FSR} \quad (\text{D.3})$$

proportional to the roundtrip time T_Φ . This leads to Eq. (5.9) for the total reflected field [41]

$$E_{ref} = E_{inc}(-r + trte^{i\Phi} + tr^3te^{2i\Phi} + \dots) = E_{inc}r \frac{e^{i\Phi} - 1}{1 - r^2e^{i\Phi}}. \quad (\text{D.4})$$

Due to the symmetry of the reflected light field it is not possible to tell just by observing the reflected signal whether the frequency needs to be increased or decreased to bring it back to resonance. Therefore the derivative of the reflected intensity, which is antisymmetric about resonance, is measured by varying the phase a little bit and observing the response of the reflected beam [45]. The phase modulated incoming signal is then given by

$$E_{inc} = E_0 e^{i(\omega t + \beta \sin(\Omega t))} \quad (\text{D.5})$$

with modulation frequency Ω and modulation index β . For small $\beta < 1$, this expression can be expanded in Bessel functions [45]

$$E_{inc} = E_0 [J_0(\beta)e^{i\omega t} + J_1(\beta)e^{i(\omega+\Omega)t} - J_1(\beta)e^{i(\omega-\Omega)t}] \quad (\text{D.6})$$

showing three components of the incident beam, the carrier at frequency ω and two sidebands at $\omega \pm \Omega$. In this approximation nearly all of the total power of the incident beam $P_0 = |E_0|^2$ is contained in the carrier $P_C = J_0^2(\beta)P_0$ and the first order sidebands are small $P_S = J_1^2(\beta)P_0$. The reflection of the modulated signal can be expressed in terms of the frequency dependent reflection coefficients $F(\omega)$ in the following way [46]

$$E_{ref} = E_0[F(\omega)J_0(\beta)e^{i\omega t} + F(\omega + \Omega)J_1(\beta)e^{i(\omega+\Omega)t} - F(\omega - \Omega)J_1(\beta)e^{i(\omega-\Omega)t}] \quad (D.7)$$

with

$$F(\omega) = \frac{E_{ref}}{E_{inc}} = r \frac{e^{i\frac{\omega}{FSR}} - 1}{1 - r^2 e^{i\frac{\omega}{FSR}}}. \quad (D.8)$$

What is actually measured is the intensity of the reflected signal [46]

$$\begin{aligned} P_{ref} &= |E_{ref}|^2 \\ &= P_C |F(\omega)|^2 + P_S [|F(\omega + \Omega)|^2 + |F(\omega - \Omega)|^2] \\ &\quad + 2\sqrt{P_C P_S} (\text{Re}[F(\omega)F^*(\omega + \Omega) - F^*(\omega)F(\omega - \Omega)] \cos(\Omega t) \\ &\quad + \text{Im}[F(\omega)F^*(\omega + \Omega) - F^*(\omega)F(\omega - \Omega)] \sin(\Omega t)) \\ &\quad + (2\Omega \text{terms}) \end{aligned} \quad (D.9)$$

consisting of the carrier wave function at frequency ω and an envelope displaying a beat pattern with two frequencies Ω and 2Ω . The sine and cosine terms oscillating at the modulation frequency Ω sample the phase of the reflected carrier and will be measured to determine the laser frequency. For low modulation frequencies the cosine term dominates, whereas for high frequencies the sine term is important. This is the signal we are interested in, therefore we isolate it by mixing the reflected with the modulation signal. If the phase between the two inputs is matched this leads to a DC-signal and we can eliminate terms oscillating at 2Ω with a low pass filter.

For fast modulation the sine term dominates and if a phase shifter compensates for time delays in the two signal paths, the phase difference will be 0° . In this case the error signal takes the form as in Eq.(5.12)[45]

$$\epsilon = -2\sqrt{P_C P_S} \text{Im}[F(\omega)F^*(\omega + \Omega) - F^*(\omega)F(\omega - \Omega)]. \quad (D.10)$$

Appendix E

Python sequence for pulse generation

```
<VARIABLES>
idle_var=self.set_variable("float","idle_var",5.000000,0.00,10000)
#freq17=self.set_variable("float","freq17",482.750000,0.1,1000000)
</VARIABLES>

<SEQUENCE>
add_to_return_list("PM Count",2)

#for i in range(1):
#seq_wait(10000)

print "_____"
print idle_var

ttl_pulse("aom_cooling",900,start_time=0,is_last=False)
ttl_pulse("aom_614",1000,start_time=0,is_last=False)
ttl_pulse("aom_prepump",100,start_time=900,is_last=False)
ttl_pulse("aom_17",2000,start_time=1002,is_last=True)
ttl_pulse("aom_cooling",2040,start_time=0,is_last=False)
ttl_pulse("gate_trig",10,start_time=20,is_last=False)
ttl_pulse("gate_trig",10,start_time=2020,is_last=True)
</SEQUENCE>
```


Danksagung

Am Ende dieser Arbeit und somit auch am Ende meines Studiums möchte ich die Gelegenheit nutzen allen Menschen zu danken die mich in den vergangenen Jahren unterstützt haben.

Bei Prof. Blatt möchte ich mich dafür bedanken, dass er sein Vertrauen in mich gesetzt hat und mir die Möglichkeit bot an einem so interessanten Projekt mitzuarbeiten. Außerdem möchte ich mich bei Markus Henrich bedanken für die freundliche Unterstützung. Ein ganz besonderer Dank gilt Gabriel Hétet und Lukas Slodička, für die gute Zusammenarbeit, die zahlreichen Diskussionen und für alles was ich von ihnen gelernt habe, aber auch dafür, dass die Arbeit mit ihnen so viel Spass gemacht hat. Weiters möchte ich mich bei allen anderen Mitgliedern der Arbeitsgruppe bedanken, dafür dass sie mich so freundlich aufgenommen haben und mir mit Rat und Tat zur Seite gestanden sind. Insbesondere möchte ich auch Patricia Moser, Thomas Holleis, Gerhard Hendl und den Mitarbeitern der Werkstätten danken.

Besonders wichtig für mich sind die Freundschaften die während meines Studiums entstanden sind. Insbesondere möchte ich Clemens Streitberger, Hannes Pichler, Matthäus Pühringer, Matthias Sassermann, Peter Cristofolini, Stephanie Fassel und Thomas Pichler danken, für das gemeinsame Lernen, Protokolle schreiben, PS-Aufgaben rechnen usw. Sie haben mich nie die Motivation verlieren lassen und dafür gesorgt dass das Studentenleben auch abseits der Uni nie langweilig wurde.

Danken möchte ich auch Bernhard, David, Astrid und meiner ganzen Familie, für ihr Verständnis und dafür, dass sie immer für mich da waren. Zuletzt möchte ich mich noch bei den beiden Personen bedanken, denen ich letztendlich alles verdanke, bei meinen Eltern Margareth und Paul. Sie haben mich stets bei allem unterstützt und an mich geglaubt, auch in den Momenten als es nicht einfach war.